



Numerical simulations of the thermal behavior of Beam Wire Scanners and energy deposition of high energy protons in carbon nanotube microbraids

Abdelrahman ABOUELENAIN

Supervisor: Dr. Federico RONCAROLO

Supervisor: Prof. Jean-Emmanuel GROETZ

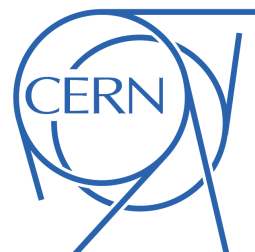
Responsible: Prof. Benoît NOYELLES

Expert: Dr. Michel DEVEL

A Thesis Submitted in Partial Fulfillment of the Requirements for the Degree of
Master of Science Physique fondamentale & applications, spécialité Physics & Computational Physics

**Université de Bourgogne Franche-Comté
Besançon, France**

The master Internship realised at
Laboratoire Chrono-environnement - Conseil Européen pour la Recherche Nucléaire



June 25, 2024



Acknowledgements

I would like to express my thanks and appreciation to Dr. Federico Roncarolo, my supervisor at CERN, for his guidance and support throughout this project. I have learned a lot about the beam instrumentation field thanks to his knowledge, enthusiasm and expertise. Thank you for your confidence and for accepting me in the Beam instrumentation group in CERN.

I could not have undertaken this journey without Prof. Jean-Emmanuel Groetz, my supervisor at the university. He has taken me in since the beginning of my master's studies and introduced me to the field and taught me the skills that are used in this work. He even introduced me to the CERN group and gave me the opportunity to attend a workshop at CERN, which was my first visit to the place. Thank you for your guidance, patience and helping me throughout the whole period.

The authors thank Dr. Mariusz Sapinski for his time, advice and work that inspired this project.

I thank Dr. Michel Devel for accepting to be included in this work as an expert.

I would like to mention Gerard Aliana Cervera, a Ph.D. student at CERN-BI for the time he spent discussing with me about the Carbon Nanotubes.

I also would like to mention Ryan Paul Camilleri, a coordination associate master student at CERN-BI, for the discussions and brainstorming we had about the thermal model of BWS which sparked ideas and helped me understand more.

I would like to acknowledge Divjot SINGH, a technical student at CERN-BI, for his help understanding PyTT.

I would like to recognize the great time I had with my colleagues in the profile measurement section at CERN-BI and general at CERN.

Thanks to my colleagues at Besancon for their great support during the good and hard times at UBFC.

أود أن أشكر أسرتي على دعمهم وحبهم لي، وأيضًا أصدقائي سواء في بيسنسون أو سيرن على الأوقات الجميلة، وبالأخص د.مصطفى حسن و د.عبدالله الأبيض اللذين كانا دعمًا حقيقيًا لي. وأيضًا أصدقائي في مصر اللذين كانوا دعمًا وتحفيزًا لبدء هذه الرحلة. أخيرًا، الحمد لله الذي أنعم علي بهذه الفرصة وأدعو أن يوفقني فيما هو آت.

عبدالرحمن محمد حلمى أبو العينين

Abdelrahman Mohamed Helmy ABOUELENAIN

Abstract

Various types of beam diagnostics are used in particle accelerators to monitor and control beam parameters such as intensity, energy, time structure, and shape. Beam Wire Scanners (BWS) belong to the class of instruments designed to measure transverse beam profiles. Thin wires are made traversing the beam at high speed (typically from 1 to 20 m/s). The beam-wire interaction produces secondary particles that can traverse the beam pipe walls and are counted by dedicated detectors, often consisting of scintillators coupled to Photo Multiplier Tubes (PMT). Correlating the wire position measurement with the secondary shower counts allows reconstructing the beam profile. During operation, BWS suffers from both peak energy deposition during a scan and integrated power, since they can result in wire sublimation and other types of damage. Assessing the damage to the BWS requires a simulation of its thermal evolution during the scan. In this work, PyTT, a Python software based on the finite difference method, has been used to evaluate the wire temperature. It takes into account beam heating and various cooling processes, including conductive, radiative, and thermionic cooling. In addition, a model was constructed using COMSOL Multiphysics and benchmark it against PyTT. The two models were used to simulate a tungsten wire, showing almost the same results with a relative difference of 1.7% at the maximum temperature. When each of the different cooling processes was simulated alone, only the conductive cooling showed different values, possibly because of differences in solving the temperature dispersion in the material between the two models.

Simulations were conducted to define scan limits (in terms of maximum beam power) at the CERN SPS for four scanners equipped with carbon fiber wires, for different beam sizes, velocities, and different combinations of beam size and intensity. Limits were defined between 1250 K and 1272 K, far from the damage limit of carbon. The carbon fiber was also simulated for a preliminary study of LHC Beam Halo monitoring applications, where the wire is placed in fixed positions at different beam sizes. The temperature of the plateau reached by the wires showed that it could be safe if the BWS is placed at a distance of 4σ from the center of the beam.

To find a solution for the wire damage problem, low-density carbon nanotubes (CNTs) are currently being investigated at CERN as a replacement for carbon fiber BWS. Energy deposition simulations of protons were conducted on some suggested samples of CNT wires with different diameters, densities, and iron impurity percentages, which result from the manufacturing process. Some types of CNT were also simulated to be compared to standard carbon fibers for the SPS scan limits and the LHC beam halo. The results showed that the cooling of the CNT wires is more effective than that of the carbon fiber, and the plateau temperature reached by the CNT wires is much lower. From the simulations, some of the wires could be used at a position 3.5σ from the center of the beam.

Contents

	Page
Acknowledgements	2
Abstract	3
Contents	4
List of Figures	7
1 Introduction	9
1.1 CERN accelerator's complex	9
1.2 Beam Diagnostics and Beam Wire Scanners	10
2 Interaction of radiation with matter	12
2.1 Stopping Power	12
2.2 Delta rays	13
2.3 FLUKA Monte-Carlo code	14
3 Heat equation	15
3.1 Beam Heating	15
3.2 Conductive Cooling	16
3.3 Radiative cooling	16
3.4 Thermionic emission	16
3.5 Cooling by Sublimation	17
4 PyTT and COMSOL	18
4.1 Simulation Input Parameters	18
4.1.1 Wire parameters	18
4.1.2 Beam parameters	20
4.2 PyTT	21
4.3 COMSOL Multiphysics	22
5 Simulations	23
5.1 Tungsten wire heating in Linac 4	23
5.2 SPS BWS operational limits	25
5.3 LHC Beam Halo	27
6 Carbon NanoTubes	30
6.1 Physical properties	30
6.2 Energy deposition	31
6.3 Thermal Behavior	33
6.3.1 SPS BWS operational Limits (with CNTs)	33
6.3.2 LHC Beam Halo (with CNTs)	35
7 Conclusion	36

Appendices	41
A Appendices	41
A Beam shape	41
A.1 Beam particles' motion	41
A.2 Beam emittance	42
B Software	45
B.1 FLUKA Monte-Carlo code	45
B.2 PyTT	46
B.3 COMSOL Multiphysics	48
C Result for SPS Beam limitations	50

List of Tables

1	The four carbon fiber BWS and the scanning conditions that they will go through in the simulations	26
2	Properties of CNT wires that are used in FLUKA simulations for energy deposition	31
3	Energy values for different densities and impurity percentages at a diameter of 5 μm	32
4	Energy values for different densities and impurity percentages at a diameter of 10 μm	32
5	Energy values for different densities and impurity percentages at a diameter of 15 μm	32
6	Energy values for different densities and impurity percentages at a diameter of 20 μm	32
7	SPS Beam limitation parameters used to scan the CNT wires	33

List of Figures

1	CERN Accelerator Complex. The particles are being accelerated until they reach their final energy for collections or being provided to other experiments [1].	10
2	(Left: Scheme of wire scanner intercepting the beam. Top right: Interaction points between the wire and the beam. Bottom right: The profile reconstruction on the vertical axis with red data points and blue Gaussian fit [2].	11
3	(a)Electronic (red dashed line), nuclear (green dashed line) and total (black continuous line) stopping power for carbon calculated for protons according to methods described ICRU Reports 37 and 49; (b) Stopping power for energy (100 MeV - 10 TeV) according to the PSTAR data up to 10 GeV (black line), simplified Bethe-Bloch equation (purple line), and Bethe-Bloch equation considering the density effect correction (red dashed line).[2] . . .	13
4	Diagram of cross sectional area of the wire S_{CS} of wire piece with length Δl . The distance travelled through the wire by the particles is represented by the yellow lines [3]	15
5	Thermionic current density J_{th} calculated using Richardson-Dushman formula [4] for carbon with work function $\phi = 4.5$ eV.	17
6	Evolution of the specific heat capacity $C_p(T)$ and thermal conductivity $k(T)$ for Carbon, Tungsten, and Iron materials. The data are collected earlier by A. Mariet, but they are based on the NIST-JANAF Thermochemical Tables, the Table of physical and chemical constant and the Handbook of physical quantities	19
7	Two estimations of the work function dependence on the temperature according to [5, 6]	20
8	Heat Flux of transverse Gaussian proton beam of $N = 1.77 \times 10^{13}$ particles with energy 450 GeV with $\sigma_x = 0.719$ mm and $\sigma_y = 0.512$ mm	21
9	Maximum Temperature of a 100 μm diameter tungsten hit by 10 pulses Linac4 160 MeV beam, $I = 70$ mA, and pulse length = 400 μm	23
10	Relative error between COMSOL and PyTT in the thermal evolution of 100 μm diameter tungsten wire as function of time for the first beam pulse. . .	24
11	Comparison of the thermal evolution considering each process alone of 100 μm diameter tungsten wire as function of time for 10 beam pulses.	25
12	Thermal evolution of BWS,41678 with different velocities, normalized emittance, and beam size	27
13	COMSOL simulations of different wire scanner fixed at different distances from beams center of sizes 200 μm and 300 μm	28
14	Sublimation of of different wire scanner fixed at the beam center and distance 1σ of beam sizes 200 μm and 300 μm	28
15	Plateau of the thermal evolution of BWS at distances 3.5 and 4 σ_s of beam sizes 200 μm and 300 μm	29
16	Plateau Temperature of BWS Versus the beam size	29
17	SEM picture of a 30 μm diameter CNT wire showing the irregularities on the surface [3][2]	31

18	CNT wires simulations for SPS Beam limitations for various diameters and densities	34
19	CNT wires simulations for SPS Beam limitations for various diameters and densities	35
20	Frenet-Serret coordinate system[7]. The red line is the reference path	41
21	(a) The motion of a single particle, at a longitudinal location s , maps an ellipse in the phase space relative to one transverse degree of freedom. The ellipse is characterized by the Courant-Snyder parameters. (b) Particles distribution in phase space. The Cartesian axes X, X' are chosen in order to minimize the sum of the square distances between the points and the axis X [8][2].	42
22	Input file for FLUKA file	46
23	Thermal evolution of BWS,41677 with different velocities, normalized emittance,and beam size	50
24	Thermal evolution of BWS,51638 with different velocities, normalized emittance,and beam size	51
25	Thermal evolution of BWS,51638 with different velocities, normalized emittance,and beam size	52

1 Introduction

Founded in 1954, the European Organization for Nuclear Research (CERN) has become the largest particle physics laboratory in the world [9]. It is located near the Franco-Swiss border near Geneva. While CERN's main focus is particle physics, aiming to unravel the mysteries of the universe, its physics program is much broader. It covers various research fields from nuclear and high-energy physics to antimatter studies and the potential effects of cosmic rays on clouds.

1.1 CERN accelerator's complex

The CERN accelerator's complex is not only conceived to serve the Large Hadron Collider (LHC), but also to provide beams to other experimental facilities, such as: Antimatter with Antiproton Decelerator (AD) and Extra Low Energy Antiproton (ELENA), Ion beam with Isotope Separator On-Line Device (ISOLDE), Neutron-nucleus interactions for a wide range of neutron energies with Neutron Time-of-Flight (n_TOF), proton-driven plasma wakefields for charged particles acceleration in Advanced WAKEfield Experiment (AWAKE), and the induced damage on materials caused by the irradiation in High Radiation to Materials (HiRadMat) [2].

The acceleration chain in the CERN complex consists of a linear accelerator and four circular accelerators:

- **Linac4**

At the beginning of the Linac4 accelerator, negative hydrogen ions H^- are produced from compressed hydrogen gas and accelerated to 160 MeV. The ions are stripped from their electrons during injection into the proton synchrtron booster (PSB) [10].

- **Proton Synchrotron Booster**

The first circular accelerator consists of four superimposed rings at the injection of which H^- are converted into protons after passing through thin carbon foils that detach electrons. After acceleration to 2 GeV, protons are transferred to the Proton Synchrotron (PS). The PSB also feeds the ISOLDE experiments [11].

- **Proton Synchrotron**

The 628 m circumference synchrotron picks up the protons from the PSB and accelerates them to 26 GeV. At that energy they undergo "γ transition in which energy added to protons is translated into addition in mass instead of velocity". PS also accelerates heavy ions from low-energy ion rings (LEIRs), feeding them to experiments or more powerful accelerators. After the protons are accelerated, they will be delivered to the Super Proton Synchrotron (SPS), or to the EAST area, AD and n_TOF [12].

- **Super Proton Synchrotron**

This 7 km circumference accelerator [13] provides the LHC with 450 GeV beams through two transfer lines (injecting in the clockwise and anti-clockwise). It also provides beams to the North Area fixed target experiment[14], HiRadMat [15] and AWAKE [16].

- **Large Hadron Collider**

The world's largest collider, with a circumference of 27 km, accelerates protons to 7 TeV per ring, resulting in a collision energy of 14 TeV. The collisions take place at four large detectors: ATLAS, CMS, ALICE, and LHCb [17].

Recently completed projects like the LHC injector upgrades (LIU) [18] and future ones like the High Luminosity LHC Project (HL-LHC) [19] or the Future Circular Collider (FCC) [20], result in higher beam brightnesses, i.e. higher beam intensities and lower beam sizes.

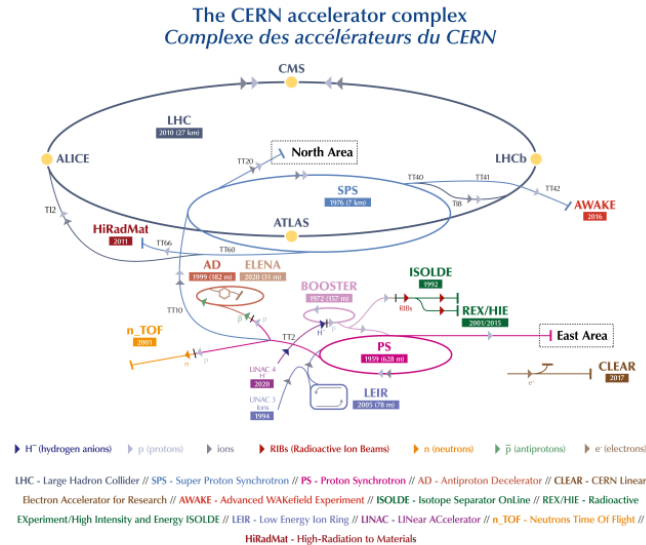


Figure 1: CERN Accelerator Complex. The particles are being accelerated until they reach their final energy for collections or being provided to other experiments [1].

1.2 Beam Diagnostics and Beam Wire Scanners

In any particle accelerator beam, instrumentation is essential to ensure safe operation, to detect problems, and improve performance. The main *observables* normally are: beam intensity, position, losses, longitudinal and transverse profiles [21].

Beam Wire Scanners (BWS) are often used as reference monitors for reconstruction of transverse beam distributions. As shown in Fig. 2, BWS consists of a thin wire moving across the beam and generating a shower of secondary particles, The transverse beam profile is reconstructed by counting the secondary particles (e.g. by means of scintillator-Photomultiplier detectors) in correlation to the wire position.

The measurement accuracy and resolution are often dominated by the wire position determination, especially in the presence of vibrations, which depend, among other effects, on wire heating, thermal cycles, and tension loss. Wire heating can occur due to direct beam energy deposition [22, 23] or by electromagnetic coupling between the beam and the BWS system. Indeed, studying and predicting wire heating is of paramount importance for BWS design and operation [2].

BWS properties or parameters that significantly affect wire heating include wire material, wire geometry (such as diameter), and wire scan speed.

Starting from the work and models presented in [23], this work focused on simulating wire heating under various beam and BWS conditions (particularly for the SPS and the LHC) using and comparing two different SW tools: the commercial product COMSOL [24] and the custom-made Python suite PyTT, also discussed in [7]. The studies were applied to both 'standard' Carbon wires (used for many years at CERN) and novel Carbon Nanotube (CNT) fibers.

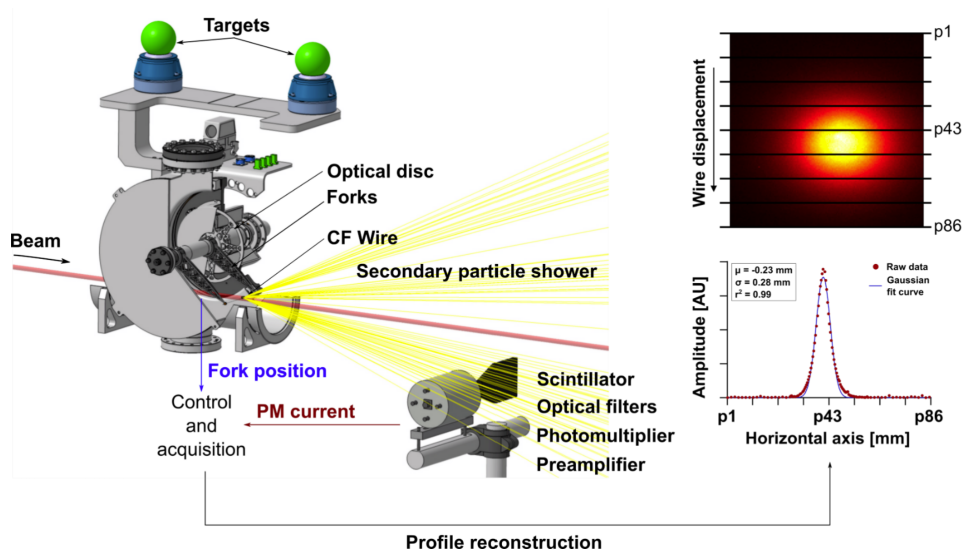


Figure 2: (Left: Scheme of wire scanner intercepting the beam. Top right: Interaction points between the wire and the beam. Bottom right: The profile reconstruction on the vertical axis with red data points and blue Gaussian fit [2].

2 Interaction of radiation with matter

The *mean free path* of a particle traversing a material can be written as

$$\lambda = \frac{1}{\Sigma} \quad (2.1)$$

Where Σ is the macroscopic cross section. It can be expressed in terms of the microscopic cross section and the density of atoms per unit volume:

$$\Sigma = n \sigma_{eff} \quad (2.2)$$

The cross section σ_{eff} is the probability that a specific process would occur over a surface area. It depends on the range of the force of the interaction between the particles, and this may vary with other variables like the energy of the particles. Processes include elastic scattering, in which the energy of the incident particle is conserved but the trajectory is modified, and inelastic scattering, which is the process in which we are interested, where the incident particle loses energy.

2.1 Stopping Power

The accelerated particle has a probability of interaction with the target's material, nuclei, and electrons. The particle loses a fraction of its energy as a result of these interactions. The stopping power includes the collision and radiation contributions of these interactions. The stopping power is the mean linear loss of energy of a particle as it goes through a material. The stopping power has electronic and nuclear contributions. At low energy, the nuclear contributions are predominant, while the electronic contributions are predominant at high energy. The processes causing this contribution depend on the irradiated target material and the nature of the incident particle. These processes include inelastic collisions with the electrons, elastic scattering with the nuclei, and some radiation, such as the Bremsstrahlung radiation effect and Cherenkov radiation. For protons, they lose their energy mainly by ionizing or exciting the atoms.

The Bethe-Bloch formula describes the stopping power $\langle \frac{dE}{dx} \rangle$ expressed in $[\text{MeV} \cdot \text{cm}^2 \cdot \text{g}^{-1}]$ of a specific material and a specific incident particle. It is the mean rate of energy loss during the travel of the particle through the medium.

$$-\langle \frac{dE}{dx} \rangle = \frac{KZ}{A} \frac{q_p^2}{\beta^2} \left[\frac{1}{2} \left(\ln \frac{2m_e c^2 \beta^2 \gamma^2 W_{max}}{I^2} \right) - \beta^2 - \frac{\delta(\beta\gamma)}{2} \right] \quad (2.3)$$

where ρ , A , Z , and I are the density, mass number, atomic number, and the mean excitation energy of the target material respectively. I varies from a few eV for materials with low Z to hundreds of eV for high Z materials [25], and now a table of experimental results of I with Z is used [26].

Since the electrons in the target could get energy from the incident particles and get excited or gain enough energy to escape from the atom's potential, the maximum energy that could be transferred to an electron can be described by W_{max} .

$$W_{\max} = \frac{2m_e c^2 (\beta\gamma)^2}{1 + 2\gamma \frac{m_e}{m_p} + \left(\frac{m_e}{m_p}\right)^2} \quad (2.4)$$

where m_e and m_p are the masses of the electron and the incident particle, respectively, while β and γ are the relativistic parameters. The parameter K in the equation (2.3) depends on the classical electron radius, the electron mass, and the Avogadro number, defined as $K = 4\pi N_A r_e^2 m_e c^2$ (where N_A is the Avogadro number and r_e is the classical electron radius). The parameter $\delta(\beta\gamma)$ is called the density correction factor, and it refers to the near saturation in the stopping power due to the a polarization effect of the high energy particles on the target.

The stopping power decreases initially with a factor of $1/\beta^\alpha$ where $\alpha = 1.7 - 1.5$, decreasing with increasing Z , and reaches a broad minimum at $\beta\gamma = 3.8 - 3.0$. After reaching the minimum, the stopping power increases by two mechanisms [26].

The first mechanism accounts for the increase in $\beta^2\gamma^2$ dependence through the relativistic flattening and extension of the particles' electric Coulomb field [26]. The electric field polarizes the medium rather than ionizes it, and atoms close to the path of the particles will produce polarization, reducing the Coulomb field acting on distant atomic electrons and reducing the energy loss in distant collisions [27], canceling the logarithmic term at high energies. This effect is accounted for in the density correction factor $\delta(\beta\gamma)$.

The other mechanism is due to the factor $\beta^2\gamma$. In the case where $2\gamma m_e \gg m_p$ in the denominator of the W_{\max} equation (2.4), the equation becomes $W_{\max} = Mc^2\beta^2\gamma$, which in turn is due to rare large energy transfers to a few electrons [26].

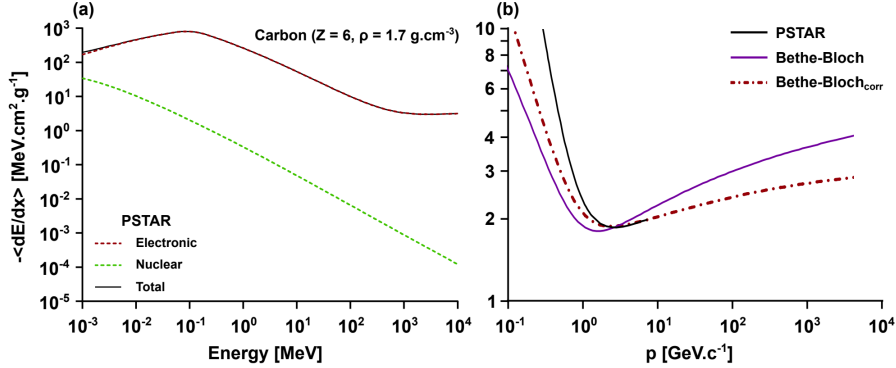


Figure 3: (a) Electronic (red dashed line), nuclear (green dashed line) and total (black continuous line) stopping power for carbon calculated for protons according to methods described ICRU Reports 37 and 49; (b) Stopping power for energy (100 MeV - 10 TeV) according to the PSTAR data up to 10 GeV (black line), simplified Bethe-Bloch equation (purple line), and Bethe-Bloch equation considering the density effect correction (red dashed line).[2]

2.2 Delta rays

When incident particles hit the wire, they can transfer energy to electrons ranging from a few hundred eV up to W_{\max} . These electrons are essentially knocked out of the material

and have enough energy to create additional secondary electrons and ionization events. The number of δ electrons produced was presented by Rossi in 1952 [28], with the distribution of electrons having kinetic energy W such that $I \ll W < W_{\max}$.

$$\frac{d^2N}{dTdx} = \frac{1}{2} K q_p^2 \frac{Z}{A} \frac{1}{\beta^2} \frac{F(W)}{W^2} \quad (2.5)$$

where $F(W)$ is a spin-dependent function that depends on the spin of the incident particles and is unity for energy $W \ll W_{\max}$. Depending on the energy of the primary particles, the δ electrons can reach an energy above 1 keV. The total δ rays produced per unit distance can be calculated by integrating (2.5) from an arbitrary lower limit to W_{\max} , as described by (2.4). These δ electrons may contribute to the total energy transported to the irradiated medium because the electrons are not part of the material after ejection, so the energy they obtain is no longer part of the energy transferred. Additionally, they can transfer energy to another electron or atom in the target medium while being ejected, adding energy to the target which is not from the incident particles.

2.3 FLUKA Monte-Carlo code

FLUKA is a versatile Monte Carlo code used for calculating particle transport and interactions with matter across various domains, from proton and electron accelerators to cosmic rays, neutrino physics, and radiotherapy. It boasts a robust framework that incorporates comprehensive and precise physical models, grounded in solid physics principles, and validated against experimental data. FLUKA's microscopic approach ensures consistency among reaction steps, enforcement of conservation laws, and faster results compared to traditional methods. It's equipped to handle intricate geometries with its improved Combinatorial Geometry (CG) package (which is a package used for particle simulation using Monte-Carlo method that allows a straightforward implementation of complicated geometric setups with intersecting boundaries, where subsequent modifications to the geometry are easily performed [29]) capable of accurately tracking charged particles even in the presence of magnetic or electric fields.

The FLUKA software package includes Flair, a graphical interface that facilitates the creation and editing of input files. Flair streamlines the editing process, minimizing errors, and offering an interactive geometry editor for visual modifications. With features for compiling, debugging, executing, and monitoring simulations, Flair ensures efficient workflow management. Moreover, FLUKA offers extensive post-processing capabilities and a library of materials and geometric objects for enhanced flexibility and collaboration. The FLUKA setup involves defining parameters such as beam characteristics, geometry, media, and scoring, allowing users to tailor simulations to their specific needs. FLUKA's versatility makes it a powerful tool for simulating energy deposition by incident beams, accounting for various interaction processes, including the effects of high-energy δ electrons.

3 Heat equation

As mentioned earlier, when the BWS interacts with a proton beam, the beam deposits a fraction of its energy into the wire. Most of this energy can be considered as heat flowing into the wire. This heat leads to a rapid increase in temperature. However, this increase in temperature is counteracted by cooling processes. The equation that models the thermal evolution was created by M. Sapinski [23], and the following equation was written by A. Navarro [7]:

$$\left(\frac{\partial T}{\partial t}\right)_{Tot} = \left(\frac{\partial T}{\partial t}\right)_{BH} - \left(\frac{\partial T}{\partial t}\right)_{CC} - \left(\frac{\partial T}{\partial t}\right)_{RC} - \left(\frac{\partial T}{\partial t}\right)_{Th} - \left(\frac{\partial T}{\partial t}\right)_{Sub} \quad (3.6)$$

where $\left(\frac{\partial T}{\partial t}\right)_{BH}$ is the beam heating, $\left(\frac{\partial T}{\partial t}\right)_{CC}$ is conductive cooling, $\left(\frac{\partial T}{\partial t}\right)_{RC}$ is radiative cooling, $\left(\frac{\partial T}{\partial t}\right)_{Th}$ is thermionic cooling, and $\left(\frac{\partial T}{\partial t}\right)_{Sub}$ is cooling due to sublimation. Since the simulations are done in vacuum environment, the convection cooling is not considered.

3.1 Beam Heating

The beam heating is the effect of the direct energy deposited on the wirescanner by the proton beam. This heating effect has been recently described by M.Boucard [3]

$$\left(\frac{\partial T}{\partial t}\right)_{BH} = \frac{\Phi(x, y, t) S_{CS}}{\rho C_p(T) V} \frac{\pi}{4} d \left\langle \frac{dE}{dx} \right\rangle \rho \quad (3.7)$$

where $\Phi(x, y, t)$ [$\text{cm}^{-2}\text{s}^{-1}$] is the flux of the incident particles, $\left\langle \frac{dE}{dx} \right\rangle$ is the stopping power of a single particle [$\text{MeV}\cdot\text{cm}^2\cdot\text{g}^{-1}$], S_{CS} is the wire's cross section, V is the volume, ρ is the density of the wire's material, and $C_p(T)$ is the heat capacity of the wire. The term $\frac{\pi}{4} d \left\langle \frac{dE}{dx} \right\rangle \rho$ represents the energy deposition on the wire, and the correction factor $\pi/4$ accounts for the fact that the distance traveled by the particles through the wire isn't always d , since the cross section of the wire is a circle. The equation is simplified to [3]:

$$\left(\frac{\partial T}{\partial t}\right)_{BH} = \frac{\Phi(x, y, t)}{C_p(T)} \left\langle \frac{dE}{dx} \right\rangle \quad (3.8)$$

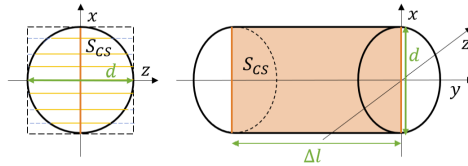


Figure 4: Diagram of cross sectional area of the wire S_{CS} of wire piece with length Δl . The distance travelled through the wire by the particles is represented by the yellow lines [3]

3.2 Conductive Cooling

Heat conduction refers to the transfer of thermal energy through direct contact between particles or objects. It occurs when there is a temperature difference between two adjacent regions in a substance, such as a wire. The region with a higher temperature transfers heat to the cooler region. This heat transfer happens because of the random motion of atoms in the wire. Atoms with more energy collide with lower energy particles, transferring their energy and raising the temperature of the cooler region. This process is governed by Fourier's law, which controls heat conduction along the wire. Heat will be transferred from the region hit by the beam to the rest of the wire. The expression for Fourier's law is as follows:

$$\left(\frac{\partial T}{\partial t}\right)_{CC} = \frac{k(T)}{\rho C_p(T)} \left(\frac{\partial^2 T}{\partial x^2} + \frac{\partial^2 T}{\partial y^2}\right) \quad (3.9)$$

where, $k(T)$ represents the thermal conductivity of the wire's material. It plays a significant role at low temperatures where radiation cooling and thermionic emission are ineffective. This process is dominant for heat evolution up to 1500 K. However, using a material with better thermal conductivity will not necessarily enhance cooling performance due to the decrease in thermal conductivity with heating.

3.3 Radiative cooling

Radiative cooling is a process in which an object or surface releases thermal energy as electromagnetic radiation. This happens when the object's temperature is higher than its surroundings, causing it to emit radiation. The rate of radiative cooling depends on the temperature difference between the object and its surroundings, the object's surface emissivity, and the object's surface area. Larger temperature differences and higher emissivity values typically result in more substantial radiative cooling. It is governed by the Stefan-Boltzmann law and is related to the temperature's fourth power:

$$\left(\frac{\partial T}{\partial t}\right)_{RC} = \frac{S \sigma_{SB} \epsilon(T)(T^4(x, y, t) - T_0^4)}{\rho C_p(T) V} \quad (3.10)$$

where S is the surface area of object or the wire, σ_{SB} is Stefan-Boltzmann constant ($5.67 \times 10^{-8} \text{ W m}^{-2} \text{ K}^{-4}$), and V is the volume of the wire. The emissivity of the material determines the surface efficiency in radiating the thermal energy, it is the ratio between the energy radiated by the material and that is radiated by a black-body. This process becomes the dominant process after the conductive cooling until the temperature approaches 3000K.

3.4 Thermionic emission

Thermionic emission refers to the emission of electrons from the surface of a material when heated. When the material reaches high temperatures, the electrons close to the surface gain sufficient energy to overcome the work function barrier $\phi(T)$ [eV], escaping into the surrounding space. This cooling process is dominant at high temperatures and can be expressed as follows:

$$\left(\frac{\partial T}{\partial t}\right)_{Th} = S(\phi + 2k_B T) \frac{J_{th}(T)}{\rho C_p(T) V} \quad (3.11)$$

where k_B is the Boltzmann constant (1.38×10^{-23} J/K), ϕ is the material's work function, and the thermionic current $J_{th}(T)$ [A cm^{-2}]. The thermionic current density is described by the Richardson and Dushman formula [4].

$$J_{th} = A_R T^2 \exp\left(\frac{-\phi}{k_B T}\right) \quad (3.12)$$

where $A_R = 4\pi m k_B^2 q_e / h^3$ is the Richardson constant, which is approximately equal to $120.173 \text{ A cm}^{-2} \text{ K}^{-2}$ (m is the electron's mass and h is Planck's constant) and ϕ is the work function. The value of the current density is nearly zero at low temperatures, but due to the temperature dependence, the current density's value becomes high with high temperatures.

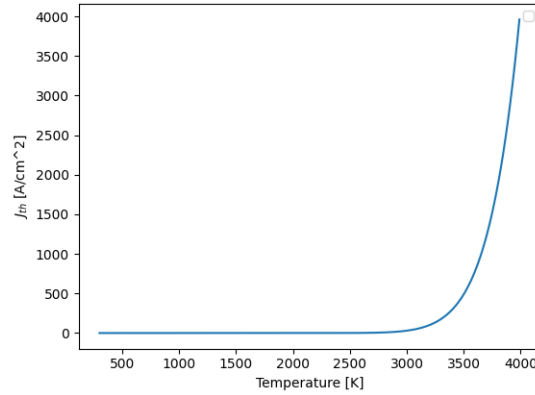


Figure 5: Thermionic current density J_{th} calculated using Richardson-Dushman formula [4] for carbon with work function $\phi = 4.5$ eV.

3.5 Cooling by Sublimation

Sublimation is a process where matter in the solid phase changes to gas without passing through the liquid phase. In order for a substance to undergo sublimation, a certain amount of energy must be provided, which is quantified by the sublimation enthalpy H_{sub} [kJ/mol] [30]. The rate of material sublimation could be estimated as described in [31]

$$\log W_{sub} = C - 0.5 \log T - \frac{B}{T} \quad (3.13)$$

where W_{sub} is the amount of sublimated material per unit area per unit time [$\text{g cm}^{-2} \text{ s}^{-1}$]. The sublimation coefficient C and B are constants and are material characteristics. This leads to the sublimation cooling to be:

$$\left(\frac{\partial T}{\partial t}\right)_{Sub} = \frac{H_{sub}}{m_{mol}} \frac{S W_{sub}(T)}{\rho C_p(T) V} \quad (3.14)$$

4 PyTT and COMSOL

PyTT (Python Thin Target) is a Python numerical model implemented by M. Sapinski and A. Navarro [32, 33]. The purpose of this model is to estimate the temperature and the signal generated by beam traversing thin targets in the form of wires, or foils. The model uses the equations discussed in Chapter 3

This chapter will discuss how PyTT has been compared to simulations performed with the COMSOL Multiphysics software (SW) suite to estimate the BWS's temperature under different operational scenarios.

4.1 Simulation Input Parameters

The following sections will summarize the wire and beam parameters to be defined as input for the wire heating studies.

4.1.1 Wire parameters

The relevant wire parameters can be summarized as:

Parameter name	Symbol
Diameter	d
Density	ρ
Specific Heat Capacity	$C_p(T)$
Thermal Conductivity	$k(T)$
Emissivity	ϵ
Work Function	ϕ

The specific heat capacity $C_p(T)$ and the thermal conductivity $k(T)$ are important parameters. $C_p(T)$ influences every heating and cooling while $k(T)$ affects only conductive cooling. As shown in Fig. 6, they both vary with temperature, as well as the emissivity ϵ , which in turn characterizes radiation cooling effects. The work function ϕ relates to thermionic cooling effects.

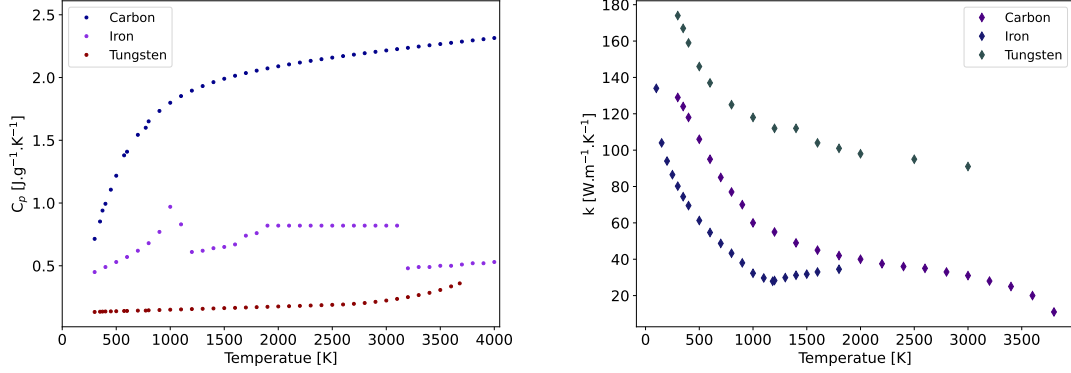


Figure 6: Evolution of the specific heat capacity $C_p(T)$ and thermal conductivity $k(T)$ for Carbon, Tungsten, and Iron materials. The data are collected earlier by A. Mariet, but they are based on the NIST-JANAF Thermochemical Tables, the Table of physical and chemical constant and the Handbook of physical quantities

Studies have been conducted by A. Navarro [7] and M. Boucard [3] on the effect of those parameters on the maximum temperature.

The relative error of the temperature increases linearly with the relative emissivity error, while the behavior of the relative temperature error is exponential with the relative error in the work function. When the work function is underestimated, the corresponding error in the temperature prediction increases exponentially. Conversely, with an overestimation of the work function's relative error, the error in the temperature prediction stabilizes. This phenomenon is due to the diminishing impact of thermionic effects at this level, rendering them negligible.

A. Navarro conducted a theoretical study on the temperature dependence of the emissivity which is started from Maxwell Plank's formula for the spectral energy distribution emitted by a blackbody

$$B_0(\lambda, T) = \frac{2hc^2}{\lambda^5} \frac{1}{\exp\left(\frac{hc}{\lambda k_B T}\right) - 1}$$

and the emissivity for a given direction and wavelength

$$\epsilon_{\lambda, \varphi, \theta} = \frac{B_{mat}(\lambda, T, \varphi, \theta)}{B_0(\lambda, T)}$$

where λ is the wavelength emitted, φ, θ are the directions of the emission in the spherical coordinates, and B_{mat} is the spectral energy distribution of the material.

M. Boucard states that the work function decreases with temperature according to [5, 6] with two different approximations (see Fig. 7). The evolution could be linear [5] or quadratic [6]. The two behaviours are tested in the following points

- Linear $\phi(T) = \phi_0(1 - \beta T)$ with $\phi_0 = 6$ eV at $T=0$ K and $\beta = 9 \times 10^{-5}$
- Quadratic $\phi(T) = \phi_0 - \gamma \frac{(k_B T)^2}{\phi_0}$ with $\phi_0 = 6$ eV at $T=0$ K and $\gamma = 180$

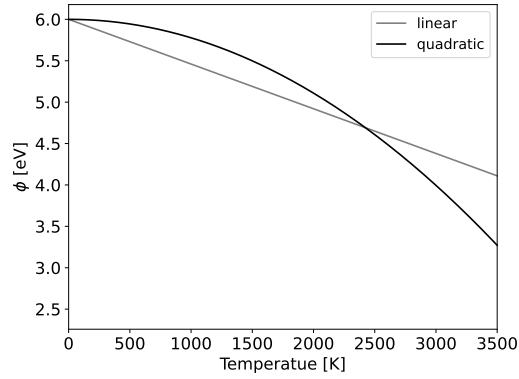


Figure 7: Two estimations of the work function dependence on the temperature according to [5, 6]

Due to the high uncertainty of the emissivity and the work function, constant values ($\epsilon=0.8$, $\phi=4.5$ eV) are used in this work. Parameters like the material's density, radius, sublimation coefficient (C , B) in equation (3.13) are also provided in [31].

4.1.2 Beam parameters

In all cases used during this work, the particle distribution has been modelled as a Gaussian distribution that can be written as:

$$N(x, y) = \frac{N_{Tot}}{2\pi\sigma_x\sigma_y} \exp \left[-\frac{1}{2} \left(\left(\frac{x-x_0}{\sigma_x} \right)^2 + \left(\frac{y-y_0}{\sigma_y} \right)^2 \right) \right] \quad (4.15)$$

where x_0 , y_0 are the position of the beam center, σ_x , σ_y are the standard deviation of the particles distribution, and $N(x, y)$ is the total number of particles in the pulse. This approximation well reproduces high energy particle beams, i.e. does not apply at the beam source front-ends and low energy linacs [7, 34].

The thermal inertia of the material is such that the microstructure of the simulated beams (in the longitudinal direction or in time) has little effect on the results. Therefore, it is enough to define beam macro-pulse length ΔT [s] and repetition rate T_R . Then one has to input the beam intensity, which can be expressed as the total number of particles N or the beam current I which are related by the pulse length.

$$N = \frac{I \cdot \Delta T}{q_e} \quad (4.16)$$

where q_e is the particle's charge.

Another fundamental input parameter is the *mass stopping power* dE/dx which is characterizing the particle energy deposition along its path in the material. It has to be put manually in COMSOL along with the input beam parameters and target material. In PyTT, a number of default cases included in the source code may need to be complemented by a manual input for specific particle / material combinations. For protons and electrons,

the stopping power can be derived from the National Institute of Standards and Technology (NIST) database [35] (for protons with energies from 10^{-3} to 10^4 MeV) or from Monte-Carlo simulations tools like FLUKA or GEANT4.

An example of particle distribution used as input for the simulations is shown in Fig. 8.

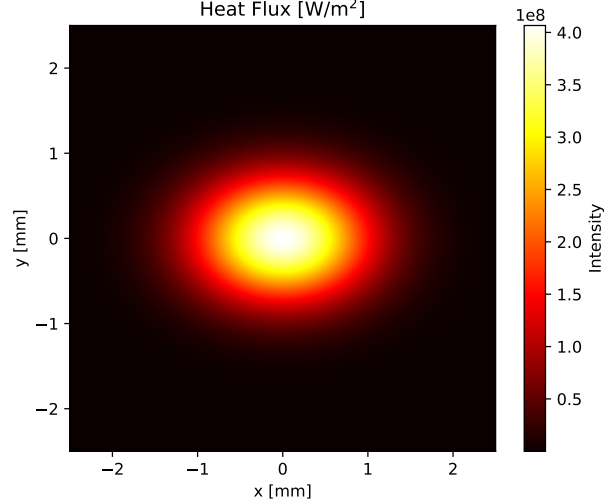


Figure 8: Heat Flux of transverse Gaussian proton beam of $N = 1.77 \times 10^{13}$ particles with energy 450 GeV with $\sigma_x = 0.719$ mm and $\sigma_y = 0.512$ mm

4.2 PyTT

PyTT is a Python package used to calculate the thermal evolution and signal generated in the wire using the Finite Difference Method, specifically the Forward in Time Centered in Space (FTCS) scheme. It assumes that the solution is known at discrete points (nodes) in the wire's geometry, with each node separated by Δx . Reducing Δx increases accuracy but also computational time. Each node i has a temperature T_i and exchanges heat with neighbors due to conductive cooling. Time discretization uses nodes m with temporal distance Δt with two values heating time (Δt_{heat}) during beam interaction and cooling time ($\Delta t_{cooling}$) where there is no interaction with the beam.

The FTCS scheme approximates time and spatial derivatives, replacing them in the heat equation considering heating, radiative cooling, and conductive cooling for sake of explanation:

$$T_i^{m+1} = T_i^m + \left[H_i^m - A_i^m ((T_i^m)^4 - (T_0)^4) + \alpha_i^m \frac{T_{i-1}^m - 2T_i^m + T_{i+1}^m}{\Delta x^2} \right] \Delta t \quad (4.17)$$

where H_i^m is beam heating, A_i^m is the radiative cooling factor, and α_i^m is heat diffusivity at the node m in time and i in space. The stability condition is:

$$\alpha \frac{\Delta t}{\Delta x^2} < \frac{1}{2} \quad (4.18)$$

The initial temperature at t^0 can be specified in PyTT or defaults to $T_i^0 = 300$ K. Boundary conditions at each time step use Dirichlet boundary conditions:

$$\begin{cases} T(0, t) = 300 \text{ K} \\ T(L, t) = 300 \text{ K} \end{cases} \quad (4.19)$$

4.3 COMSOL Multiphysics

COMSOL Multiphysics is commercial SW that is used to simulate various physical phenomena, formulated as differential equations. It employs the Finite Element Method (FEM) for spatial discretization, partitioning the domain into smaller regions called elements, with nodes at their intersections. The differential equation is approximated at each node using polynomial test functions. FEM can handle domains of arbitrary shapes, and accuracy is improved by increasing the number of elements or using higher-order polynomial functions. These basis functions are equal to one at their respective nodes and zero otherwise [36].

The procedure, based on [24], involves multiplying both sides of the heat equation by a test function ψ_j and integrating over the domain. The approximate temperature T_h is expressed using basis functions ψ_i . This transforms the heat equation into a system of equations, solved for unknown coefficients T_i . Temporal discretization uses the backward difference formula (BDF), with automatic control of BDF order and step length, varying between second and fifth orders.

$$\begin{aligned} \sum_i \frac{\partial T_i}{\partial t} \int_{\Omega} \psi_i \psi_j dS &= \int_{\Omega} H(\sum_i T_i \psi_i) \psi_j dS - \int_{\Omega} A((\sum_i T_i \psi_i)^4 - (T_0)^4) \psi_j dS \\ &\quad - \sum_i T_i \int_{\Omega} \alpha \nabla \psi_i \cdot \nabla \psi_j dS. \end{aligned} \quad (4.20)$$

where the coefficients a_k and B are constant and are chosen according to the maximum possible order k and it could be found in [37] [38]. PyTT and COMSOL are discussed with more details in appendix B

5 Simulations

This section will discuss the various specific simulations carried out to characterize the thermal response of BWS under different beam conditions and operational scenarios.

5.1 Tungsten wire heating in Linac 4

In this first example a tungsten BWS is assumed to be installed in Linac4 for thermal load analysis. a 100 μm diameter tungsten wire ($\Delta t_{cooling}$) the center of the CERN Linac4 beam ($\Delta t_{cooling}$) (beam energy 160 MeV), for 10 consecutive ($\Delta t_{cooling}$) beam pulses. The beam sizes are $\sigma_x = 2$ mm and $\sigma_y = 1$ mm. The beam has a current I of 70 mA, a pulse length of 400 μs , and a repetition period of 1.2 s. Figure 9 shows the simulated temperature evolution of the tungsten wire. After 10 pulses, the temperature decreased to 714.4 K in COMSOL and 755.7 K in PyTT after reaching a maximum of 3599.85 K in COMSOL and 3659.7 K in PyTT, with a relative difference of 1.7% between the two values. The maximum temperature reached is close to the melting point of tungsten.

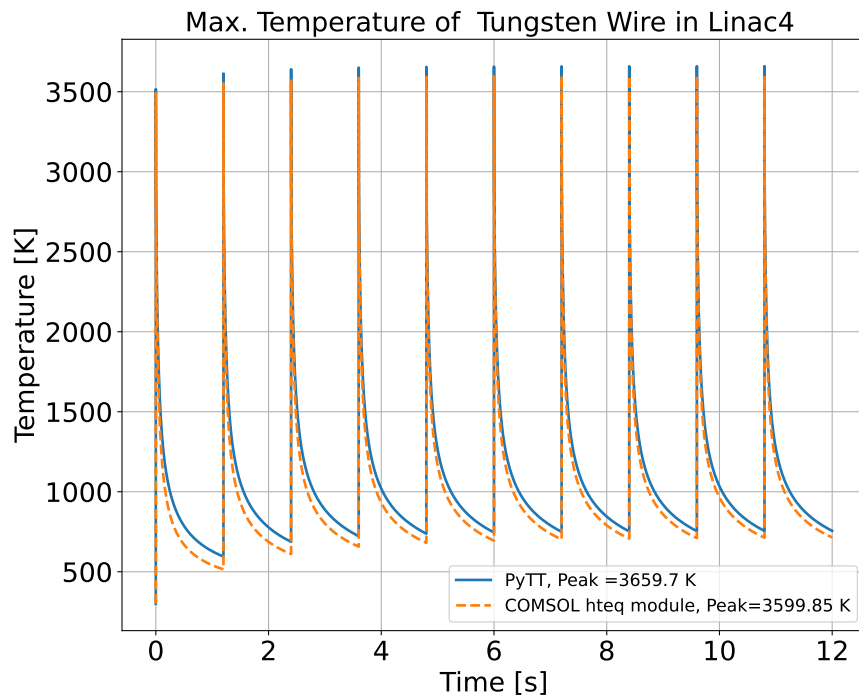


Figure 9: Maximum Temperature of a 100 μm diameter tungsten hit by 10 pulses Linac4 160 MeV beam, $I=70$ mA, and pulse length = 400 μs .

The major difference observed is in the cooling time after the pulse is vanished. The relative error between the two models is examined during the first pulse. During the heating time, the relative error is reaching a maximum of approximately 0.61% but during the cooling time it reaches a maximum of 17.55%.

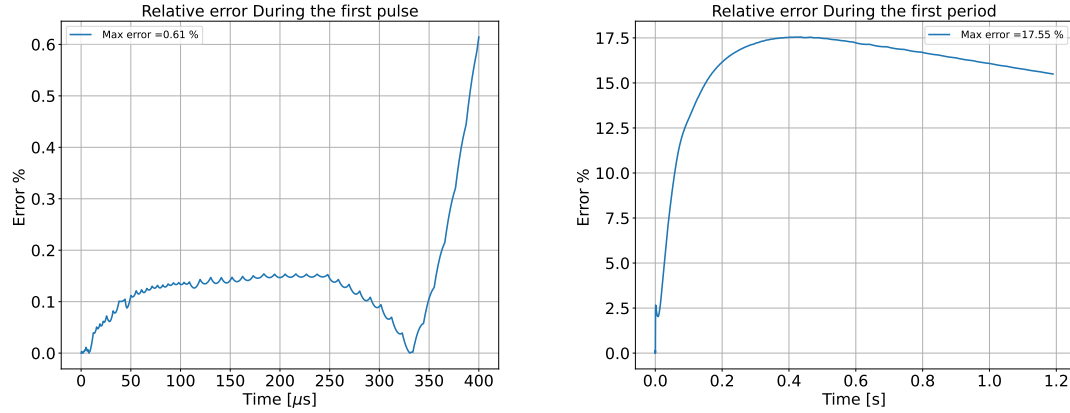


Figure 10: Relative error between COMSOL and PyTT in the thermal evolution of 100 μm diameter tungsten wire as function of time for the first beam pulse.

For the same simulation example, each process was analyzed individually to understand the distinct impacts. First, beam heating is simulated without any cooling processes in both models, and it exhibits consistent behavior and results. The radiation cooling and thermionic cooling cases also show similar behavior, though with different results for thermionic cooling.

When considering radiative cooling alone, the difference in maximum temperature between the models is less than 2 K, with a minimum temperature of 981.1 K. For thermionic cooling, the difference in maximum temperature is about 148 K, corresponding to a relative error of 4%. The difference in minimum temperature is 2.7 K (2116.4 K in PyTT and 2122.5 K in COMSOL) with a relative error of 0.29%.

The case of considering conductive cooling alone differs from both radiative and thermionic cooling. With conductive cooling as the sole active process, the energy that entered the wire could not escape from it and the total energy trapped in the wire is accumulated after each pulse. The accumulated energy is translated into a higher reached temperature and a higher minimum temperature. For instance, during the fourth pulse, the maximum temperature reaches 3845.3 K in COMSOL and 4006.3 K in PyTT, while the minimum temperature is 1215.2 K in COMSOL and 1743.9 K in PyTT. By the last pulse, the maximum temperature is 4113.8 K in COMSOL and 4408.2 K in PyTT, and the minimum temperature is 1892.6 K in COMSOL and 2811.7 K in PyTT.

The differences in temperatures can be explained by the extent of temperature dispersion from the center of the wire (where the beam impacts) to the rest of the wire via conduction. The dispersion in COMSOL is more significant compared to PyTT. The difference in dispersion could be interpreted due to the fact that the BWS in PyTT is considered as a 1D object, while the BWS is a 2D object in COMSOL allowing the temperature to disperse more freely than in just one direction for a 1D object.

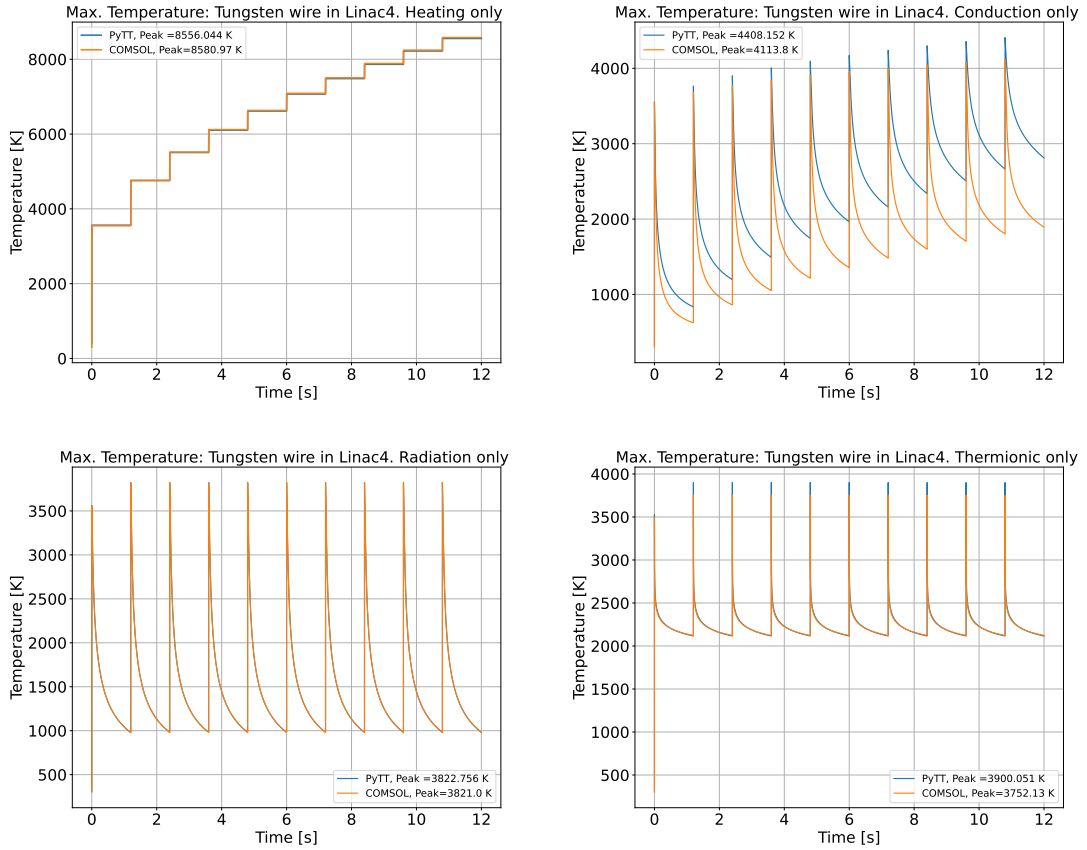


Figure 11: Comparison of the thermal evolution considering each process alone of 100 μm diameter tungsten wire as function of time for 10 beam pulses.

5.2 SPS BWS operational limits

The SPS synchrotron is equipped with 4 BWS systems, all based on 34 μm carbon wires, travelling with velocities between 5 and 20 m/s into the beam. To avoid wire damage, operational limits were put in place since many years, based on simulations and experiments [39], which lead to the general semi-empirical limit of 2.8×10^{13} protons/mm to avoid sublimation and 5×10^{12} protons/mm to avoid any wire damage due to thermal effects and fatigue.

The simulation tools developed in this work, were used to estimate the temperature evolution of wires when this last limit is applied, which can be reached under different combinations of beam size, beam intensity and wire speed.

Based on the aforementioned studies, the maximum number of particles considered as 'safe to scan' can be written as:

$$N_{max} = \frac{5 \cdot 10^{12} v t_{rev} \sigma_{tr}}{d} \quad (5.21)$$

where $t_{rev} = 2.3 \times 10^{-5}$ [s] is the revolution time of the beam, v is the velocity, σ_{tr} is the physical beam size in a direction transverse to the scan, and d is the wire's diameter. The

values of N_{max} below are calculated for a diameter of $30 \mu m$, which means that using these values for scanning with $34 \mu m$ would provide a worse scenario.

Each of the four wires, their scan direction and velocity with the beam parameters they are scanning are tabulated below.

BWSRC	σ_x [mm]	σ_y [mm]	Speed [m/s]	Nmax [E+13]
BWSRC,41677 Scan: Vertical	0.322862068	0.37940895	9	1.11
	0.322862068	0.37940895	18	2.23
	0.456595916	0.536565283	5	0.88
	0.456595916	0.536565283	9	1.58
	0.559213506	0.657155579	5	1.07
	0.559213506	0.657155579	9	1.93
BWSRC,41677 Scan: Vertical	0.318381598	0.384452997	9	1.10
	0.318381598	0.384452997	18	2.20
	0.450259574	0.543698642	5	0.86
	0.450259574	0.543698642	9	1.55
	0.551453104	0.665892124	5	1.06
	0.551453104	0.665892124	9	1.90
BWSRC,51637 Scan: Horizontal	0.420509426	0.291497818	9	1.01
	0.420509426	0.291497818	18	2.02
	0.594690133	0.412240168	5	0.79
	0.594690133	0.412240168	9	1.42
	0.728343691	0.504889031	5	0.97
	0.728343691	0.504889031	9	1.74
BWSRC,51638 Scan: Horizontal	0.415196991	0.295611834	9	1.02
	0.415196991	0.295611834	18	2.04
	0.587177215	0.418058265	5	0.80
	0.587177215	0.418058265	9	1.44
	0.719142283	0.512014716	5	0.98
	0.719142283	0.512014716	9	1.77

Table 1: The four carbon fiber BWS and the scanning conditions that they will go through in the simulations

Figure 12 shows examples of temperature evolution, representative of how the calculated limits for all systems are safe for operation. Other examples can be found in the appendix C

The results in all the simulations vary between 1250 K and 1272 K, indicating promising results that the wire should not be sublimated, and the wire could scan the beam safely in all of these scenarios and conditions. These simulations do not take into account the RF coupling heat, which it is know to be significant with the combination of beam spectrum with BWS tank resonant structures result in electro-magnetic field coupling between the beam and the wire. The thermal evolution produced by this phenomenon should be added to the thermal evolution due to the beam interaction to verify the safety of the BWS. Also in this case, the COMSOL and PyTT agreement is very good.

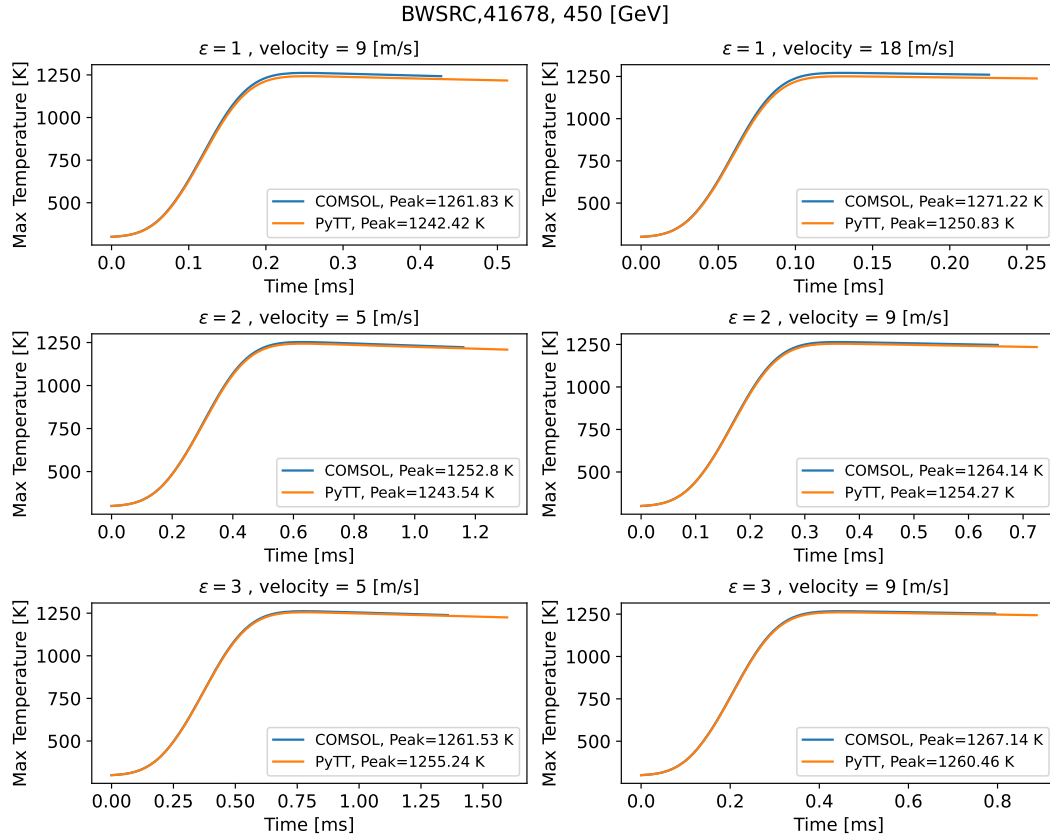


Figure 12: Thermal evolution of BWS,41678 with different velocities, normalized emittance, and beam size

5.3 LHC Beam Halo

At LHC the ideal Gaussian distribution of particles can often 'degenerate' to non Gaussian shapes as, due to different phenomena, single protons can diffuse away from the beam core and populate the so-called 'beam halo'.

This can perturb operation, as the beam halo can interact with the beamline structures, producing unwanted energy deposition or, for example, heating the superconducting magnets.

A general characteristic of the beam halo is the increase in the population of the outer part of the beam [40], but it does not have a precise definition that separates it from the core of the beam. Monitoring the beam halo is therefore of high importance and using low density thin detectors is an option under study. In this section, BWS samples are simulated at distances (static) $(3.5, 4) \sigma$ from the beam center and gives a very preliminary study of the wire heating at the beam halos.

A $34 \mu\text{m}$ carbon fiber wire is placed at the center and distances of $(1,2,3,4) \sigma_s$ of two beams, of sizes $200 \mu\text{m}$ and $300 \mu\text{m}$, each of 4.2×10^{14} protons with energy 7 TeV. The LHC beam revolution period is $89 \mu\text{m}$

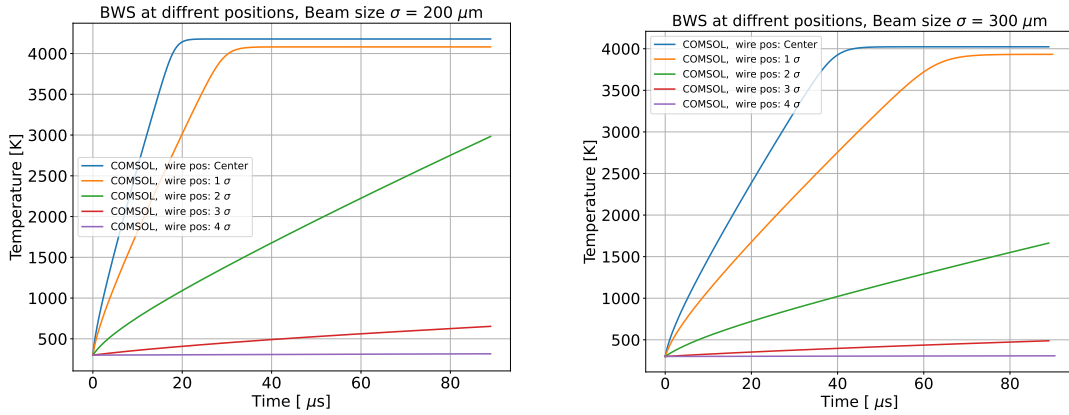


Figure 13: COMSOL simulations of different wire scanner fixed at different distances from beams center of sizes $200\mu m$ and $300\mu m$

The results are shown in Fig. 13. One can conclude that the BWS cannot withstand (as expected) an interaction with the beam while being at the center or at distances of 1σ for both sizes, and 2σ for a beam size of $200\mu m$.

Figure 14 shows the sublimation of the wires fixed at the center and at a distance of 1σ , which results in reduction of the wires' radii according to equation (3.13).

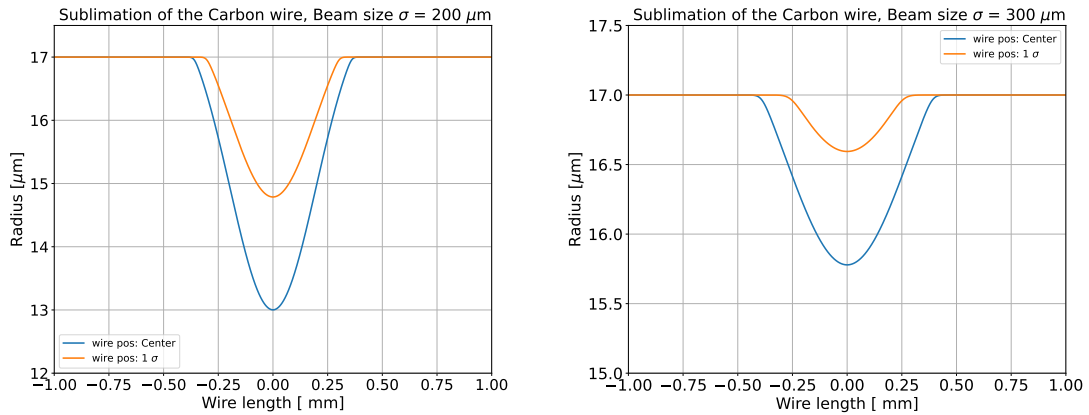


Figure 14: Sublimation of of different wire scanner fixed at the beam center and distance 1σ of beam sizes $200\mu m$ and $300\mu m$

Since the interest lies in distances of 3.5 and 4 sigmas, an extension to the above simulations was made to observe when the temperature at those distances reaches a plateau. At a distance of 3.5 sigmas, a plateau is reached at 3140.35 K for a beam size of $200\mu m$ after 0.05 s, and for a beam size of $300\mu m$, a plateau is reached at 2936.17 K after 0.1 s. For a distance of 4 sigmas, the plateau is reached at 1930.49 K for a size of $200\mu m$ and at 1582.25 K for a size of $300\mu m$.

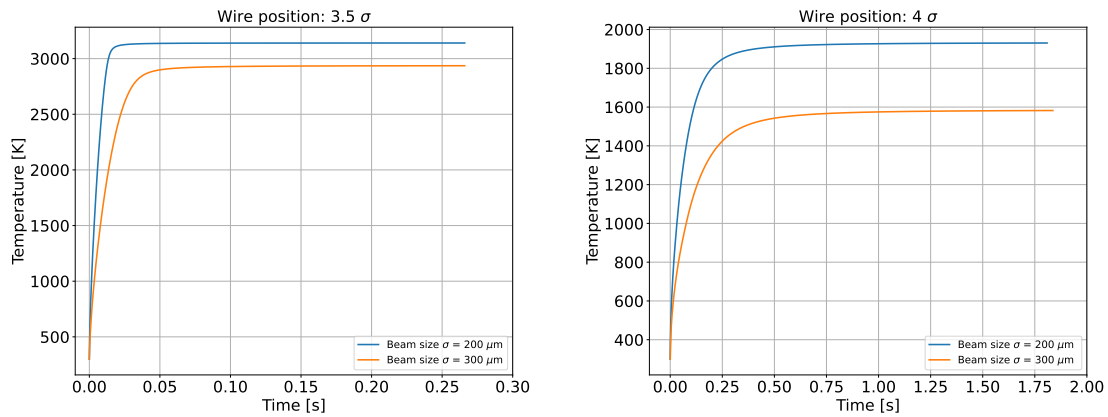


Figure 15: Plateau of the thermal evolution of BWS at distances $3.5\sigma_s$ and $4\sigma_s$ of beam sizes $200\mu m$ and $300\mu m$

Extending to the beam size of $400\mu m$, the temperature is seen to be decreased during the increasing of the beam size as the density of particles hitting the wire would decrease as the size increase it can be concluding to say it could be safe to put the wire at distance 4σ (excluding RF heating) in case of monitoring the beam halo.

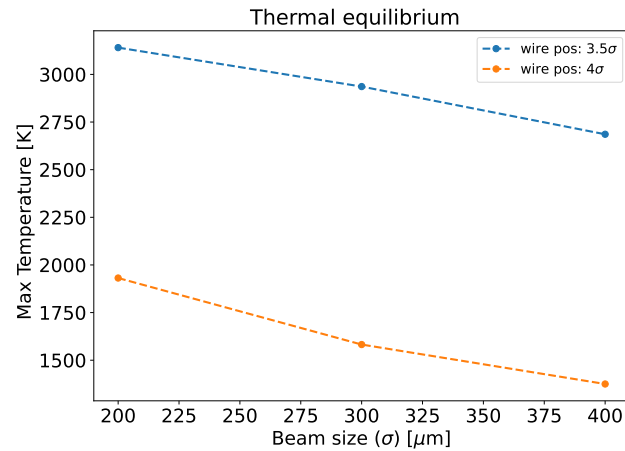


Figure 16: Plateau Temperature of BWS Versus the beam size

6 Carbon NanoTubes

The current beam wire scanners, such as tungsten (in Linacs) and carbon (in Synchrotrons) fibers, are chosen for their electrical, mechanical, and thermal properties. However, as already discussed for the SPS BWS, in all cases their operation is not possible above certain beam power thresholds, due to overheating. Introducing low-density materials could be a good solution to overcome this problem. Among these materials, carbon nanotubes (CNTs) are under study. CNTs' density depend on the manufacturing process. In this chapter, some physical properties of CNTs are briefly discussed, and then the thermal behavior of CNTs will be examined.

6.1 Physical properties

The manufacturing processes used to produce CNTs require other materials, such as catalysts or substrates, which can lead to the production of CNTs with impurities from these materials. One of these common impurities is iron, which is the only impurity considered in this report. The presence of impurities makes the CNT wires a mixture compound instead of a pure carbon material. Due to the lack of data on CNTs and the presence of impurities, approximations are made to determine some of its physical quantities as combinations of its constituent elements.

Density: The effective density of a CNT wire is given by

$$\frac{1}{\rho_{CNT}} = \frac{p_C}{\rho_C} + \frac{p_{Fe}}{\rho_{Fe}} \quad (6.22)$$

where p_C and p_{Fe} are the fractions of carbon and iron in the wire respectively. The density of iron (7.85 g/cm^3) is larger than the density of carbon ρ_C , which means that an increase in the fraction of the iron impurity would increase the density of the CNT wire, affecting the cooling processes.

Thermal properties: The specific heat and thermal conductivity of the CNT wire are assumed to be

$$C_p(T)_{CNT} = p_C \times C_p(T)_C + p_{Fe} \times C_p(T)_{Fe} \quad (6.23)$$

$$k(T)_{CNT} = p_C \times k(T)_C + p_{Fe} \times k(T)_{Fe} \quad (6.24)$$

Emissivity: The used value of the emissivity is 0.8, which is the same as that of carbon fibers. However, the emissivity is a quantity that depends on the surface of the material, and since CNTs have surface irregularities, the emissivity could have lower [3].

Work function: The used value of the work function is 4.5 eV, the same as carbon fibers. Due to the irregularities in the surface of the wire, the work function value may vary. The value is assumed to be constant because the behavior of the work function with temperature is not known for carbon fibers, and no data is available regarding CNTs.

Atomic number Z: The atomic number is used to calculate the energy deposited, but due to the presence of iron, the empirical formula for the effective atomic number is used [41]:

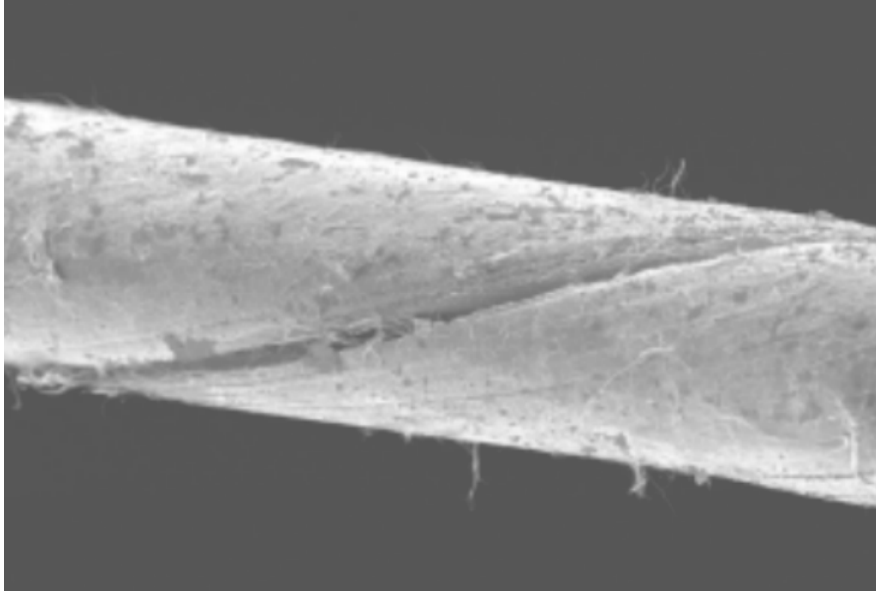


Figure 17: SEM picture of a 30 μm diameter CNT wire showing the irregularities on the surface [3][2]

$$Z_{eff} = \frac{\sum_{i=1}^n \left(\frac{p_i Z_i}{M_i} \right)}{\sum_{i=1}^n \left(\frac{p_i}{M_i} \right)} \quad (6.25)$$

6.2 Energy deposition

FLUKA simulations have been completed for several CNT wires with different diameters, densities, and impurity percentages in the wire, in line with an ongoing doctoral project conducted by Gerard Aliana Cervera on post-treatment of the CNTs. The main FLUKA inputs are summarized in Table 2.

Property	Values
Carbon Density (g/cm^3)	0.5, 1, 1.5, 2
Diameter (μm)	5, 10, 15, 20
Percentage of Impurities (%)	1, 2, 4, 6, 8
Energy (GeV)	450

Table 2: Properties of CNT wires that are used in FLUKA simulations for energy deposition

Diameter 5 μ m		Impurity					
		0.01	0.02	0.04	0.06	0.08	0.1
Density (g/cm ³)							
0.5		271.5 eV	273.2 eV	278.2 eV	283.4 eV	288.7 eV	294 eV
1		534.9 eV	539.3 eV	548.7 eV	556.9 keV	567.5 keV	576.9 eV
1.5		0.797 keV	0.802 keV	0.815 keV	0.827 keV	0.84 keV	0.854 keV
2		1.055 keV	1.063 keV	1.08 keV	1.093 keV	1.11 keV	1.125 keV

Table 3: Energy values for different densities and impurity percentages at a diameter of 5 μ m

Diameter 10 μ m		Impurity					
		0.01	0.02	0.04	0.06	0.08	0.1
Density (g/cm ³)							
0.5		556.7 eV	561.9 eV	570.8 eV	581.1 eV	595.8 eV	603.8 eV
1		1.1 keV	1.109 keV	1.127 keV	1.146 keV	1.168 keV	1.187 keV
1.5		1.638 keV	1.65 keV	1.673 keV	1.701 keV	1.727 keV	1.755 keV
2		2.176 keV	2.189 keV	2.219 keV	2.254 keV	2.285 keV	2.319 keV

Table 4: Energy values for different densities and impurity percentages at a diameter of 10 μ m

Diameter 15 μ m		Impurity					
		0.01	0.02	0.04	0.06	0.08	0.1
Density (g/cm ³)							
0.5		0.848 keV	0.871 keV	0.871 keV	0.885 keV	0.902 keV	0.919 keV
1		1.680 keV	1.692 keV	1.719 keV	1.751 keV	1.784 keV	1.810 keV
1.5		2.502 keV	2.519 keV	2.559 keV	2.604 keV	2.639 keV	2.683 keV
2		3.322 keV	3.347 keV	3.396 keV	3.440 keV	3.504 keV	3.543 keV

Table 5: Energy values for different densities and impurity percentages at a diameter of 15 μ m

Diameter 20 μ m		Impurity					
		0.01	0.02	0.04	0.06	0.08	0.1
Density (g/cm ³)							
0.5		1.142 keV	1.149 keV	1.173 keV	1.195 keV	1.218 keV	1.240 keV
1		2.266 keV	2.273 keV	2.320 keV	2.360 keV	2.400 keV	2.445 keV
1.5		3.383 keV	3.405 keV	3.453 keV	3.514 keV	3.562 keV	3.624 keV
2		4.488 keV	4.516 keV	4.590 keV	4.646 keV	4.722 keV	4.783 keV

Table 6: Energy values for different densities and impurity percentages at a diameter of 20 μ m

The FLUKA results (corrected for the term $(\frac{\pi}{4}d\frac{dE}{dx}\rho)$ discussed in Section 3.1) are shown in Table 3, 4, 5, 6.

From the results, the effect of the diameter, impurity, and density on the total energy deposition is shown. The total energy deposition increases almost linearly with the diameter

and the density, as expected. On the other hand, the impurity has less impact on the energy deposition. It's important to note that FLUKA treats the CNT wires as a homogeneous material, not necessarily reproducing the real cases. Related to this, the wire could be damaged due to the contamination in it, as shown in A. Mariet's work [2], but still, it is a good method to simulate the thermal behavior in the wire.

6.3 Thermal Behavior

Some of the simulations carried out for 'standard' wires, were repeated with samples of CNT wires, based on the total energy deposition calculated above. Two kinds of simulations were completed: one with varying wire diameters and the other with varying densities. For varying diameters, the fixed carbon density used is 0.5 g/cm^3 , while for varying density, the fixed diameter used is $10 \text{ }\mu\text{m}$.

6.3.1 SPS BWS operational Limits (with CNTs)

A set of simulations were dedicated to revisit the SPS BWS limits. The simulation input parameters are listed in Table 7 and the results are shown in Fig. 18. For SPS scans with the parameters in the first row in Table 7 at a speed of 18 m/s with varying diameters, the cooling process is slower than the beam heating process. This results in the maximum temperature reached by all the CNT wires being in the same range as the carbon fiber wires. However, at lower speed (5 m/s), the cooling process is faster. As a result, the wires reach a maximum temperature lower than that of the carbon fiber wires.

Regarding density, a simulation was conducted with parameters in the second row at a speed of 5 m/s . Similar to the varying diameter case, as the density decreases, the maximum temperature also decreases. The importance of lower diameters and densities lies in the cooling phase after the interaction with the beam. The lower diameter and density wires cool faster, as observed in the simulations. This is due to the surface-to-volume ratio and the inversely proportional relationship with density in the cooling processes.

σ_x [mm]	σ_y [mm]	Speed [m/s]	Nmax [E+13]
0.322862068	0.37940895	18	2.23
0.456595916	0.536565283	5	0.88

Table 7: SPS Beam limitation parameters used to scan the CNT wires

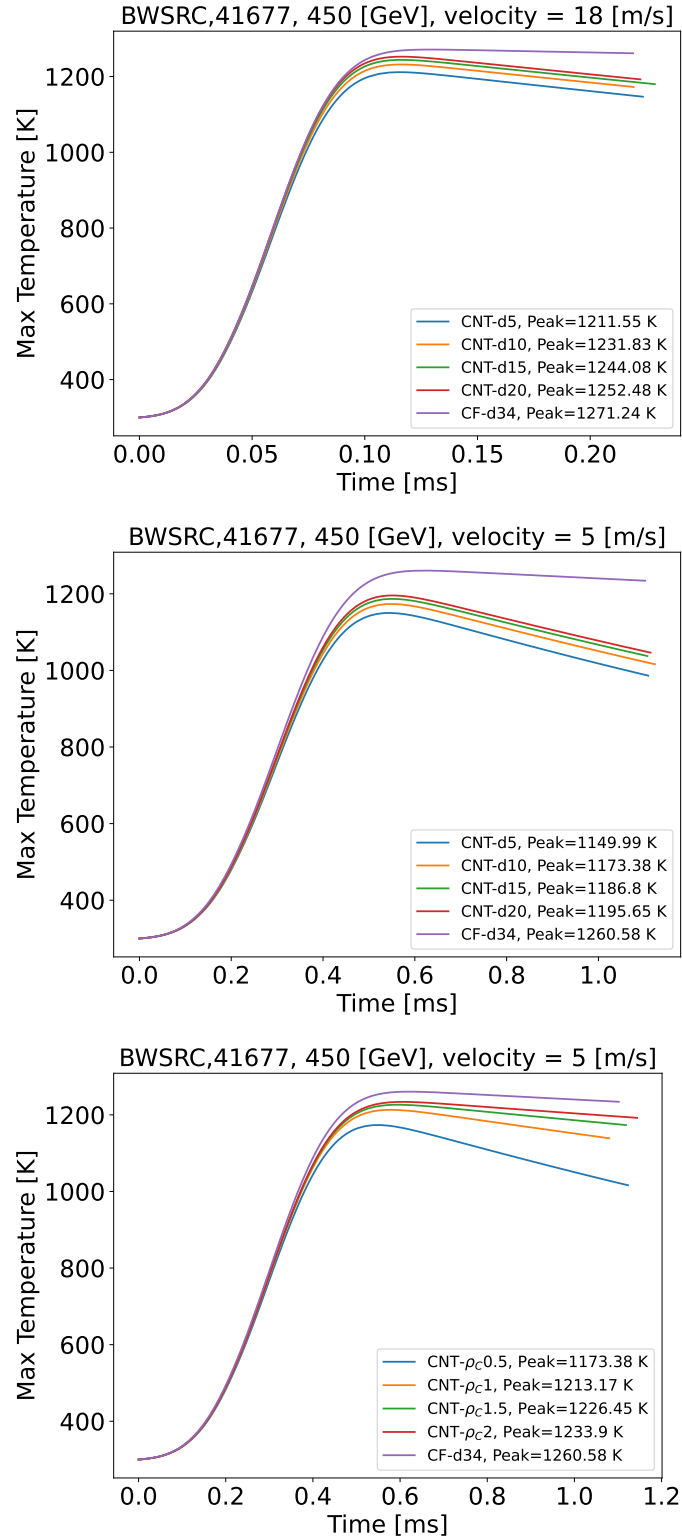


Figure 18: CNT wires simulations for SPS Beam limitations for various diameters and densities

6.3.2 LHC Beam Halo (with CNTs)

The beam halo simulations were also revisited for CNT wires. Two FLUKA simulations have been conducted for the total energy deposition from the LHC beam on two CNT wires with a diameter of $10\ \mu\text{m}$ and the following parameters: (1) Carbon density of $2\ \text{g}/\text{cm}^3$ and impurity of 0.1, and (2) Carbon density of $0.5\ \text{g}/\text{cm}^3$ and impurity of 0.01. The results were $557.48\ \text{eV}$ and $2.327\ \text{keV}$, respectively, which are similar to the ones obtained from the SPS energy deposition. These energy depositions from the table above were used in the simulations.

The same wires were used as in the SPS limitations. The simulations were conducted to reach the plateau of the thermal evolution at a distance of $3.5\ \sigma$ for a beam size of $300\ \mu\text{m}$. The results are shown in Fig. 19. CNT wires offer a significant advantage over carbon fiber due to their lower temperature characteristics. When comparing the temperature of a carbon fiber wire at $2936.17\ \text{K}$ to the maximum temperatures of CNT wires shown in red (diameter = $20\ \mu\text{m}$, $\rho_C = 0.5\ \text{g}/\text{cm}^3$ in the first plot and diameter = $10\ \mu\text{m}$, $\rho_C = 2\ \text{g}/\text{cm}^3$ in the second plot), which are $1651.42\ \text{K}$ and $2352.26\ \text{K}$ respectively, it is evident that the CNT wires' temperature decreases with a decrease in diameter or density. This makes CNT wires more suitable than carbon fiber wires for Beam Halo applications.

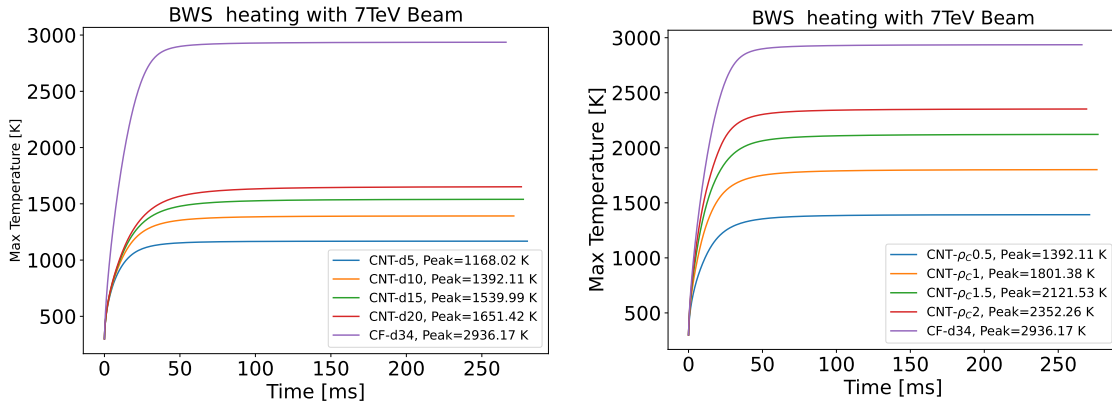


Figure 19: CNT wires simulations for SPS Beam limitations for various diameters and densities

7 Conclusion

The aim of this work was to build a COMSOL Multiphysics model to evaluate the thermal behavior of a beam wire scanner and benchmark it against the custom-made Python Thin Target (PyTT) package currently in use. Additionally, thermal studies for new suggested safe scan limits in the SPS accelerator and preliminary studies on BWS behavior while monitoring the Beam Halo in the LHC were conducted, along with an examination of low-density CNTs for BWS applications.

A 2D COMSOL model was built using the same non-linear differential formula as in A. Navarro’s thesis [7], which is used in PyTT. The model considers a number of beam and BWS parameters. The beam parameters include the number of protons in the beam, the beam size, and the assumed Gaussian transverse beam profile. The BWS parameters include the material density, specific heat, thermal conductivity, and the wire’s diameter. As discussed in Chapter 2, the energy deposition of the proton on BWS, i.e. the heat source, is described by the Bethe-Bloch formula that quantifies the energy loss or stopping power of a particle passing through matter. The FLUKA Monte-Carlo code was utilized to calculate the energy loss in the BWS. It also takes into account the δ -ray electrons that escape the wire with some of the deposited energy.

Firstly, the model was benchmarked against PyTT with a fixed tungsten wire exposed to 10 pulses of a Linac4 160 MeV energy beam. The results were in agreement, with a relative difference of 1.7% at the maximum reached temperature and of 0.06% at the minimum temperature. Further analysis was conducted by considering each cooling process alone. Simulations of radiative and thermionic cooling processes showed agreement within 4%. The simulated contribution of conductive cooling was stronger in COMSOL than in PyTT because the wire is treated as a 2D object in COMSOL while it’s treated as a 1D in PyTT, affecting the temperature dispersion in the two models.

The simulation tools were utilized to determine the maximum temperatures that the SPS BWS could reach when applying different beam parameters. Past studies identified these as the upper limit in beam power necessary to ensure wire integrity. The simulations replicated a scan at various operational speeds, up to 20 m/s. In all instances, the maximum temperature fell within the range of 1250 K and 1272 K, which is considered safe for carbon fibers.

This work then included a preliminary study of the use of thin wires to measure LHC beam halo. The simulated model consisted in placing wire samples at different (static) position, defined in units of beam size σ away from the beam core. This was repeated for different absolute beam sizes. When positioning the wire at 1σ temperatures are unacceptables and wire sublimates. For distances between 3 and 4σ , the peak temperatures are predicted to be lower and some cases (wire positions at 3.5 and 4σ and beam sizes of 200, 300, and 400 μm) were studied in detail in order to precisely determine the equilibrium temperature. The temperatures at a distance of 3.5σ were high, in the range of about 3100 K to 2750 K (unacceptable), whereas at a distance of 4σ they were found to be in the range of 1950 K to 1300 K (cases potentially suitable).

Low-density materials are examined as a candidate to replace *classical* carbon fibers. These include Carbon Nano tubes (CNT). CNTs feature good mechanical and thermal properties, but it must be noted that thermal simulations accuracy is affected by the lack of precise and confirmed data. Energy deposition studies for suggested CNT characteristics,

such as densities, impurity percentages, and diameters, was conducted. The results indicate an increase in total energy deposition with an increase in diameter and density. An increase in impurity also results in a rise in energy deposition, but not as significantly as the other two characteristics.

Some of the SPS scan limits were tested with sample CNT wires. With high velocities, the maximum temperatures reached are similar to the carbon fiber wire as the cooling processes are slower than the beam heating. However, with lower velocities, the cooling processes start to catch up, and the maximum temperature begins to decrease. The maximum temperature decreases with decreasing diameter and density, and the cooling is much faster with lower diameter and density. CNT wires were also examined for beam halo utilization, showing a huge advantage over carbon fiber wire as they show much lower plateau temperatures. All of this adds to the credibility of low-density materials for beam instrumentation applications.

The results described above, which were achieved in the timescale of this master project, could be further expanded in the future. Possible ideas and examples include:

- Considering the RF coupling between the beam and BWS, and examine its thermal effects to fully understand BWS wire thermal evolution during operation.
- Conducting more detailed study of the beam halo and beam profile, including the beam halo shape, for a more accurate thermal behavior of BWS.
- Carrying out experimental studies on the work function and emissivity of carbon fiber and CNT, along with other CNT properties approximated in this report.
- Developing a 3D COMSOL model where cooling processes other than conductive cooling are treated as surface boundary cooling processes, rather than as a heat sink in less dimensional models.

References

- [1] CERN accelerator complex. URL: <https://home.cern/science/accelerators/accelerator-complex>.
- [2] Alexandre MARIET. *Study of the effects of copper-coating and proton irradiation at 440 GeV on the mechanical properties of carbon nanotube wires for particle beam*. PhD thesis, University of Bourgogne Franche-Comté, May 2023.
- [3] Manon Boucard. *Thin targets in extreme conditions: probing high-brightness hadron beams*. Master's thesis, École Polytechnique Fédérale de Lausanne, September 2023.
- [4] O. W. Richardson. Electron emission from metals as a function of temperature. *Phys. Rev.*, 23:153–155, Feb 1924.
- [5] Adam Kiejna, Kazimierz F. Wojciechowski, and J Zebrowski. The temperature dependence of metal work functions. *Journal of Physics F: Metal Physics*, 9:1361–1366, 1979.
- [6] Reza Rahemi and Dongyang Li. Variation in electron work function with temperature and its effect on the young's modulus of metals. *Scripta Materialia*, 99:41–44, 2015.
- [7] A. Navarro Fernandez. *Understanding Secondary Emission Processes and Beam Matter interactions for Optimization of Diagnostic Wire Grid System in Particle Accelerators*. PhD thesis, Universitat Politècnica de Catalunya, September 2022.
- [8] F. Roncarolo. *Accuracy of the Transverse Emittance Measurements of the CERN Large Hadron Collider*. PhD thesis, Milan Polytechnic, September 2005.
- [9] Wikipedia contributors. CERN — Wikipedia, the free encyclopedia. URL: <https://en.wikipedia.org/w/index.php?title=CERN&oldid=1232724344>, 2024.
- [10] Linac4. URL: <https://home.cern/science/accelerators/linear-accelerator-4>.
- [11] The Proton Synchrotron Booster. URL: <https://home.cern/science/accelerators/proton-synchrotron-booster>.
- [12] The Proton Synchrotron. URL: <https://home.cern/science/accelerators/proton-synchrotron>.
- [13] The Super Proton Synchrotron. URL: <https://home.cern/science/accelerators/super-proton-synchrotron>.
- [14] CERN SPS North Area Experiments. URL: https://scientific-info.cern/archives/history_CERN/Exp-Programme-02#SPS-NA.
- [15] CERN High-Radiation to Materials (HIRADMAT) facility. URL: <https://hiradmat.web.cern.ch/>.
- [16] CERN Advanced Proton Driven Plasma Wakefield Acceleration Experiment (AWAKE). URL: <https://home.cern/science/accelerators/awake>.

- [17] The Large Hadron Collider. URL: <https://cds.cern.ch/record/2809109/files/CERN-Brochure-2021-004-Eng.pdf>.
- [18] Klaus Hanke, H. Damerau, A. Deleu, A. Funken, Roland Garoby, S.S. Gilardoni, N. Gilbert, Bethany Goddard, E.B. Holzer, Alessandra Lombardi, Django Manglunki, M. Meddahi, Bettina Mikulec, Elena Shaposhnikova, and M. Vretenar. Status of the LIU project at CERN. pages 3397–3399, 07 2014.
- [19] The HL-Large Hadron Collider. URL: <https://home.cern/resources/faqs/high-luminosity-lhc>.
- [20] The Future Circular Collider. URL: <https://fcc.web.cern.ch/overview>.
- [21] Sara Benítez Berrocal. *Design and Development of an Optical Beam Loss Monitor Based on Cherenkov Light Detection for the CERN Super Proton Synchrotron Accelerator*. PhD thesis, University of Huddersfield, September 2022.
- [22] Mariusz Sapinski, Bernd Dehning, Ana Guerrero, Jan Koopman, and Elias Métral. Carbon fiber damage in accelerator beam. Technical report, CERN, Geneva, Switzerland, May, 2018.
- [23] M Sapinski. Model of Carbon Wire Heating in Accelerator Beam. Technical report, CERN, Geneva, 2008.
- [24] COMSOL Multiphysics cyclopedia. URL: <https://www.comsol.com/multiphysics/finite-element-method#discret2>.
- [25] Benjamin Cheymol. *Development of beam transverse profile and emittance monitors for the CERN LINAC4*. PhD thesis, Université Clermont-Ferrand II - Blaise-Pascal, December 2011.
- [26] R.L. Workman et al. (Particle Data Group). Review of Particle Physics. *Progress of Theoretical and Experimental Physics*, 2022(8):549–563, August 2022.
- [27] Young S. Kim. Density effect in dE/dx of fast charged particles traversing various biological materials. *Radiation Research*, 56(1):21–27, 1973.
- [28] Bruno Benedetto Rossi. *High-energy particles*. Prentice-Hall physics series. Prentice-Hall, New York, NY, 1952.
- [29] Fragoso M, Seco J, Nahum AE, and Verhaegen F. Incorporation of a combinatorial geometry package and improved scoring capabilities in the EGSnrc Monte Carlo Code system. *Medical physics*, 30(6), 1076–1085, 2003.
- [30] Heat of sublimation. URL: [https://chem.libretexts.org/Bookshelves/Physical_and_Theoretical_Chemistry_Textbook_Maps/Supplemental_Modules_\(Physical_and_Theoretical_Chemistry\)/Thermodynamics/Energies_and_Potentials/Enthalpy/Heat_of_Sublimation](https://chem.libretexts.org/Bookshelves/Physical_and_Theoretical_Chemistry_Textbook_Maps/Supplemental_Modules_(Physical_and_Theoretical_Chemistry)/Thermodynamics/Energies_and_Potentials/Enthalpy/Heat_of_Sublimation).
- [31] S. Dushman. *Scientific foundations of vacuum technique*. Wiley Inc, New York 1966.

- [32] A. Navarro Fernandez's PyTT page. URL: <https://github.com/navarrof/PyTT>.
- [33] M. Sapinski's PyTT page. URL: <https://github.com/ClaudePP/PyTT>.
- [34] Helmut Wiedemann. *Particle accelerator physics*. Springer Nature, 2015.
- [35] S. Seltzer. Stopping-power and range tables for electrons, protons, and helium ions. *NIST Standard Reference Database*, 1993.
- [36] Jonathan Whiteley. *Finite Element Methods*. Springer Nature, February 2017.
- [37] Jeff R. Cash. *Backward Differentiation Formulae*, pages 97–101. Springer Berlin Heidelberg, Berlin, Heidelberg, 2015.
- [38] Backward differentiation formula. URL: https://en.wikipedia.org/wiki/Backward_differentiation_formula.
- [39] M Sapinski. Beam Interaction with Thin Materials: Heat Deposition, Cooling Phenomena and Damage Limits. *Conf. Proc.*, C1204151:WECP04, 2012.
- [40] T. P. Wangler and K. R. Crandall. Beam halo in proton linac beams. *eConf*, C000821:TU202, 2000.
- [41] R. MURTY. Effective atomic numbers of heterogeneous materials. *Nature*, 207:398–399, 1965.
- [42] *An Introduction to the Physics of High Energy Accelerators*, pages 287–288. John Wiley & Sons, Ltd, 1993.
- [43] W. T. Weng and S. R. Mane. Fundamentals of particle beam dynamics and phase space. *AIP Conference Proceedings*, 249(1):3–45, 03 1992.
- [44] E.D. Courant and H.S. Snyder. Theory of the alternating-gradient synchrotron. *Annals of Physics*, 281(1):360–408, 2000.
- [45] Alfredo Ferrari, Paola R. Sala, Alberto Fass'ò, and Johannes Ranft. Fluka: multi-particle transport code. Technical report, CERN and INFN, 2024.

A Appendices

A Beam shape

In this section some of the beam characteristics will be briefly discussed like the beam particles motion, the transverse beam profile, the phase space of the beam and the beam emittance which could be used to determine the beam size in the transverse plane. This section is based on [7, 2, 8].

A.1 Beam particles' motion

The motion of the particles in the beam is described in the Frenet-Serret coordinate system, a coordinate system that is used to describe the kinematic properties of particles moving in a differentiable curve. As shown in Fig. 20, the longitudinal coordinate (S) is tangent to the called reference path which the path of the ideal beam, while X and Y describe the transverse plane normal to the trajectory. The term $\rho(s)$ is the curvature of the reference path and terms $x(s)$ and $y(s)$ describe the deviation from reference path.

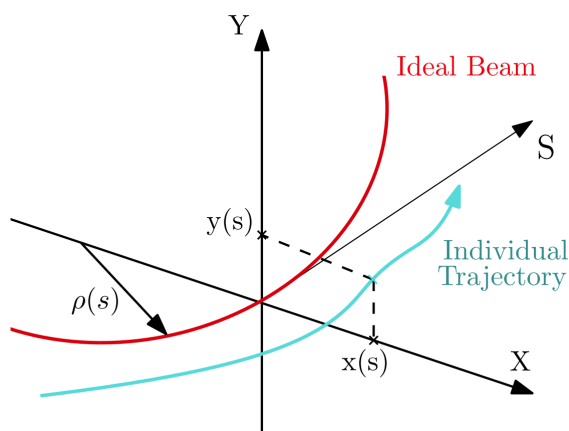


Figure 20: Frenet-Serret coordinate system[7]. The red line is the reference path

The particles inside the accelerator has to be guided around the reference path while being accelerated to the desired energy and this could be done by applying electromagnetic forces described by Lorentz force

$$\mathbf{F} = q(\mathbf{E} + \mathbf{v} \times \mathbf{B}) \quad (\text{A.26})$$

where q is the the charge of the particle and \mathbf{v} is velocity vector of the particles which are being accelerated by the longitudinal electric field \mathbf{E} , bent and focused by the transverse magnetic field \mathbf{B} .

Due to the focusing and bending of the magnetic field, the particle that has a non-zero transverse coordinate and momentum starts to perform oscillations as it moves in the trajectory [42]. The motion of the particles in the transverse space can be described by

differential equations which describe the motion of pseudo-harmonic oscillator with a spring constant depending on position (s)[43], in the form of

$$x'' + \left(\frac{1}{\rho^2(s)} + \frac{1}{B\rho} \frac{\partial B_y(s)}{\partial x} \right) x = 0$$

$$y'' - \frac{1}{B\rho} \frac{\partial B_y(s)}{\partial x} y = 0$$
(A.27)

where $B\rho$ is called the magnetic rigidity and it comes from the equilibrium between the centrifugal and the centripetal Lorentz forces with ρ the radius of the circular machine and the product equals to the ration of the momentum to the charge p/q .

A.2 Beam emittance

The status of the particles are described by their position and velocity. However, not only do the particles have different positions, but also they have different velocity directions. The velocity of a particle can be divided into longitudinal velocity (in the beam direction) and transverse velocity (normal to the beam direction). The transverse velocity can be broken down into components in the X and Y axes. Phase spaces between the position and the velocity in each axis, x and y, contain all the information of the particles, which would form an elliptical distribution.

It's convenient for the calculation to consider two axes X', X in this example centered at the barycenter of the distribution and oriented to minimize the square distance between each point and each axis.

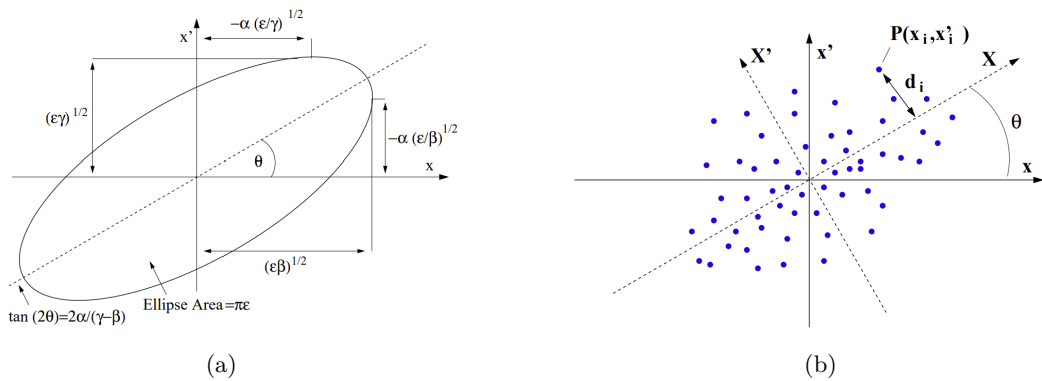


Figure 21: (a) The motion of a single particle, at a longitudinal location s , maps an ellipse in the phase space relative to one transverse degree of freedom. The ellipse is characterized by the Courant-Snyder parameters. (b) Particles distribution in phase space. The Cartesian axes X, X' are chosen in order to minimize the sum of the square distances between the points and the axis X [8][2].

The distance of particle i from the X axis will be

$$d_i = |x'_i \cos \theta - x_i \sin \theta|$$
(A.28)

Where θ is the rotation angle of the X axis to x and is defined by minimizing the distance d

$$\frac{d}{d\theta} \left(\frac{1}{N} \sum_{i=1}^N d_i^2 \right) = \frac{d}{d\theta} \sigma_X = 0 \quad (\text{A.29})$$

This leads to

$$\tan 2\theta = \frac{2\overline{xx'}}{\overline{x^2} - \overline{x'^2}} \quad (\text{A.30})$$

with

$$\overline{x^2} = \frac{1}{N} \sum_{i=1}^N x_i^2 \quad (\text{A.31})$$

$$\overline{x'^2} = \frac{1}{N} \sum_{i=1}^N x_i'^2 \quad (\text{A.32})$$

$$\overline{xx'} = \frac{1}{N} \sum_{i=1}^N x_i x_i' \quad (\text{A.33})$$

The value of θ defines the orientation of X' to be $\theta + \frac{\pi}{2}$ giving two orthogonal axes X and X' . the variances of the particles distances from X and X' are

$$\sigma_X = \frac{1}{2} \left(\overline{x^2} + \overline{x'^2} + \frac{2\overline{xx'}}{\sin 2\theta} \right) \quad (\text{A.34})$$

$$\sigma_{X'} = \frac{1}{2} \left(\overline{x^2} + \overline{x'^2} - \frac{2\overline{xx'}}{\sin 2\theta} \right) \quad (\text{A.35})$$

The variances of the particle distribution in the phase space diagram can be assigned as semi-axes of the beam envelope ellipse of equation

$$\frac{X}{\sigma_X} + \frac{X'}{\sigma_{X'}} = 1 \quad (\text{A.36})$$

The area of the ellipse $A = \pi\sigma_X\sigma_{X'}$ and we can define the beam emittance(the spread of the particle distribution in the phase space).

$$\varepsilon = \frac{A}{\pi} = \sigma_X\sigma_{X'} \quad (\text{A.37})$$

The ellipse could be written with respect to axes x and x'

$$x^2\sigma_{x'} + 2xx'r\sigma_x\sigma_{x'} + x'^2\sigma_x = \sigma_x^2\sigma_{x'}^2 \quad (\text{A.38})$$

where σ_x , $\sigma_{x'}$ are the standard deviations and $r = \overline{xx'}/\sqrt{\overline{x^2}\overline{x'^2}}$ is called the correlation coefficient.

The Courant-Snyder parameters $(\alpha_{cs}, \beta_{cs}, \gamma_{cs})$ are a set of quantities that are used to describe the distribution of particles in a phase space on a given axis. They are introduced by Ernest Courant and Hartland Snyder in their 1953 [44] and are related to σ_X , $\sigma_{X'}$ in the following notion:

$$\sigma_X = \sqrt{\beta_{cs}\varepsilon} \quad (\text{A.39})$$

$$\sigma_{X'} = \sqrt{\gamma_{cs}\varepsilon} \quad (\text{A.40})$$

$$4r\sigma_X\sigma_{X'} = \alpha_{cs}\varepsilon \quad (\text{A.41})$$

with relation between the parameters equals to

$$\beta_{cs}\gamma_{cs} - \alpha_{cs}^2 = 1 \quad (\text{A.42})$$

Using these equations alongside with (A.37), (A.38) becomes:

$$\varepsilon = \gamma_{cs}x^2 + 2\alpha_{cs}xx' + \beta_{cs}x'^2 \quad (\text{A.43})$$

This equation explains the concept of the beam emittance as the area of ellipse defined by the particle dispersion.

For a beam with Gaussian distribution in the transverse plane, the distribution's standard deviation varies with the betatron function $B_{cs}(s)$ which represents the modulation amplitude due to the changing focus strength. The beam size decreases with the energy. When considering a particle's standard deviation in the transverse distribution and neglecting the beam dispersion, we can calculate the horizontal and vertical size of the complete beam at a specific position (s).

$$\sigma_{b(h,v)} = \sqrt{\beta_{cs(h,v)}(s) \varepsilon_{(h,v)}(s)} \quad (\text{A.44})$$

The beam size is calculated using the normalized emittance $\epsilon_{norm} = \epsilon\beta\gamma$, which is determined by the operational condition of the machines and ideally should be constant during acceleration and whatever the beam energy. The beam size decreases as the beam energy increases, so combining the normalized emittance relation with equation (A.39) one can get the beam size

$$\sigma = \sqrt{\frac{\epsilon_{norm}\beta_{cs}}{\beta\gamma}} \quad (\text{A.45})$$

B Software

In this section a few details about the software used are provided

B.1 FLUKA Monte-Carlo code

The FLUKA code is a general-purpose Monte Carlo code. It is a tool used for calculations of particle transport and interactions with matter, covering an extensive range of applications spanning from proton and electron accelerators to cosmic rays, neutrino physics, and radiotherapy. The code is built and maintained to include the most comprehensive and precise physical models[45]. In this "microscopic" approach, each step is grounded in solid physics, microscopy models are adopted whenever possible, consistency among all the reaction steps and/or reaction types is ensured, conservation laws are enforced at each step, and results are checked against experimental data at a single interaction level. This algorithm yields quicker results than compiling particle production data at a single interaction level[2].

FLUKA can handle even very complex geometries, using an improved version of the well-known Combinatorial Geometry (CG) package. The FLUKA CG has been designed to correctly track charged particles, even in the presence of magnetic or electric fields.

FLUKA has a graphical interface named Flair. It is used to facilitate the creation and editing of the FLUKA input file. Flair has several beneficial features, such as a user-friendly front-end interface that minimizes errors during editing, validation, and error correction of the input file. It also has an interactive geometry editor for visually editing bodies and regions, complete with real-time debugging information. Additionally, it has capabilities for compiling, debugging, executing, and monitoring the status during a run. There is a back-end interface for post-processing output files and generating plots through interaction with gnuplot. Moreover, there is a library of materials and geometric objects to simplify editing, storing, and sharing among other users and projects [45].

FLUKA is set up by building an input file, which allows the user to determine and describe in pseudo-code the main parameters of the simulation [21]. These inputs are:

- **Beam characteristics**

The beam position and direction within the geometry, the transverse and longitudinal distribution, and the particle type, its energy or momentum, and the number of primary starting particles.

- **Geometry**

The components of the environment are defined here. Each geometry is a combination of simple bodies (rectangles, cylinders, planes, etc.), and one or more simple bodies can be grouped to form a region. The particle interactions, energy deposition, and other processes can be assigned and monitored in these regions.

- **Media**

A material must be assigned to each region. FLUKA has a database of materials, including pure elements and compounds. Additionally, the user can define their own material by specifying properties such as density, atomic number, mass number, and even compounds by adding the elements that comprise it and the percentage of each element.

- **Scoring**

The FLUKA code is used to obtain statistical estimations of several quantities. Scoring provides cards to estimate these quantities. The spatial distribution of the energy deposited or the total fluence in a mesh or the energy deposited in a region is provided using the USRBIN card. The DETECT card is used to count the incident particles and the energy deposited by them. The AUXSCORE card is used to filter the data the user wants by the type of desired quantity (e.g., energy) and the type of particle that produces the quantity (e.g., proton, electron, etc.). Tracking of the particles in a region can be provided by USRTRACK or USERDUMP cards.

- **Executable routines**

The user can modify the basic code to obtain specific data or results about the interaction that is not provided by the standard cards. These modified routines are executed during the run of the simulation as specified by the SOURCE card.

The FLUKA Monte Carlo code will be used for simulating the energy deposition by the incident beam on the wire, as it can handle the transport of charged particles, taking into account the processes mentioned above and others (particle-nucleus interaction, photon interactions, etc.). Energy deposition by the incident protons is not only described by the Bethe-Bloch formula (2.3), but also the high-energy δ electrons have to be considered.

```

TITLE
SPS_450MeV_d2_rho2_imp4
* Set the defaults for precision simulations
DEFAULTS
* Define the beam characteristics
BEAM -450. 0.0 0.0 -1.PROTON
*HI-PROPE 82. 208.
DETECT 0.2 1E-6 1E-4 wire1Edepot1
DETECT 0.0 1E-6 1E-3 wire1Edepot2
USRBIN 10. PROTON -21. 0.1 0.1 40.beamprot
USRBIN -0.1 -0.1 -10. 100. 100. 200. &
USRBIN 10. PROTON -22. 20. 20. 70.fluprot
USRBIN -20. -20. -50. 200. 200. 200. &
USRBIN 10. ENERGY -23. 0.002 0.25 10.002Ewire
USRBIN -0.002 -0.25 9.998 10. 10. 10. &
USRBIN 10. ENERGY -24. 0.002 0.05 10.002Ewire1
USRBIN -0.002 -0.05 9.998 50. 100. 50. &
USRBIN 10. PROTON -25. 20. 20. 25.tankprot
USRBIN -20. -20. -5. 200. 200. 200. &
USRBIN 10. ELECTRON -26. 20. 20. 25.tankelec
USRBIN -20. -20. -5. 200. 200. 200. &
*USRYIELD 123. ALL-PART -27. wire1 tank_in LETall
*USRYIELD 0.5 0.1 100. 440.
*USRYIELD 123. PROTON -27. wire1 tank_in LETprot
*USRYIELD 0.5 0.1 100. 440.
*USRYIELD 123. ELECTRON -27. wire1 tank_in LETelec
*USRYIELD 0.5 0.1 100. 440.
*USRYIELD 123. PHOTON -27. wire1 tank_in LETphot
*USRYIELD 0.5 0.1 100. 440.
*USRBIN 10. DPA-SCD -28. 0.002 0.5 10.002DPAwire1
*USRBIN -0.002 -0.5 9.998 50. 100. 50. &
*USRBIN 12. DPA-SCD -29. wire1 DPAtot
*USRBIN wire1 -30. 7. wire1 resnuc
*RESNUCLE 12. ENERGY -31. wire1 Etotwire
USRBIN wire1 12. ENERGY -40. wire1 Eprotwi
USRBIN wire1 12. ENERGY -41. wire1 Elecwi
AUXSCORE USRBIN PROTON Eprotwi
USRBIN 12. ENERGY -41. wire1 Elecwi
USRBIN wire1 ELECTRON Elecwi
*USRTRACK -1. ELECTRON -32. tank_in 500.Eelec
*USRTRACK 150. 1E-7 500. tank_in 500.EHI
*USRTRACK 0.1 1E-4 500. wire1 500.EHIw
*USRTRACK -1. HEAVYION -34. wire1 500.EHIw
*USRTRACK 0.1 1E-4 500. wire1 tank_in fluHI
*USRBDX 99. HEAVYION -35. wire1 tank_in 1.
*USRBDX 0.1 1E-4 500. 500.
*USRTRACK -1. PIONS+-36. tank_in 500.Epions
*USRTRACK 100. 1E-3 500. &
*USRTRACK -1. PIONS+-36. wire1 500.Epionsw
*USRTRACK 100. 1E-3 500. &
*USRBDX 99. PIONS+-37. wire1 tank_in flupions
*USRBDX 100. 1E-2 500. 1.
*USRTRACK -1. ALL-PART -38. tank_in 500.Eall
*USRTRACK 200. 1E-7 500. &
*USRBDX 99. ALL-PART -39. wire1 tank_in flual1
*USRBDX 200. 1E-7 500. 1.
RANDOMIZ
STEPSIZE 0.000001 1. wire1
FLUKAFIX 0.01 graphwir
IONTRANS HEAVYION 1. graphwir
MULSOPT 1. 2000.GLOBAL
DELTARAY 1E-7 graphwir
PHYSICS 2.
PHYSICS 3. 1000. EM-DISSO
*PHYSICS 1. EVAPORAT
PHYSICS 1. DPMTHRES
PHYSICS 1. COALESCE
* Define the beam position
BEAMPOS 0.0 0.0 -50.
* Set the number of primary histories to be simulated in the run
START 50000.
GEOBEGIN 1. COMBNAME
0 0
RPP BLK -110 110. -110 110. -110 110.
RPP ROOM -100. 100. -100. 100. -100. 100.
RCC TUBE1_EX 0.0 0.0 -99. 0.0 0.0 99.1 5.5
RCC TUBE1_IN 0.0 0.0 -98. 0.0 0.0 98.1 5.
RCC TUBE2_EX 0.0 0.0 19.9 0.0 0.0 80. 5.5
RCC TUBE2_IN 0.0 0.0 19.9 0.0 0.0 80. 5.
#if 0
RCC SCINT -15. -2.5 100. 0.0 5. 0.0 1.5
#endif
RPP TANK_EX -15. 15. -15. 15. 0.0 20.
RPP TANK_IN -14.9 14.9 -14.9 14.9 0.1 19.9
RCC WIRE30 0.0 -9. 10. 0.0 18. 0.0 0.00005
    
```

Figure 22: Input file for FLUKA file

B.2 PyTT

PyTT is a python package use to calculate the thermal evolution and the signal generated in the wire. The package uses Finite difference method to solve the non-linear second-order differential heat equation for the thermal evolution, especially the Forward in Time Centered in Space scheme(FTCS).

It goes under the assumption that only the solution is known at a number of points or nodes in the geometry of the wire; each node is separated with it's adjacent nodes by distance Δx in space and decreasing Δx leading to more accurate results, but on the other hand, it will increase the computational time as the equation will be solved for more nodes. Each node i will have a temperature T_i and can exchange heat with it's neighbours due to the conductive cooling.

The temperature changes with time, so the solution for the heat equation has to be also time discretized, so the time nodes m will have a temporal distance Δt . In the program there are two values, one for the heating time (Δt_{heat}) when the beam is interacting with the wire and one for cooling time ($\Delta t_{cooling}$) when there is no interaction and the wire is cooling down. This is the case when the wire is fixed and not moving and the beam is pulsed.

B.2.1 Forward in Time Centered in Space scheme

The procedure is as mentioned by A.Navarro[7], and the FTCS scheme approximates the time derivative and the spatial derivative as follows:

$$\left. \frac{\partial T}{\partial t} \right|_{t^m, x_i} = \frac{T_i^{m+1} - T_i^m}{\Delta t} - \mathcal{O}(\Delta t) \quad (\text{A.46})$$

$$\left. \frac{\partial^2 T}{\partial x^2} \right|_{x_i} = \frac{T_{i-1}^m - 2T_i^m - T_{i+1}^m}{\Delta x^2} - \mathcal{O}(\Delta x^2) \quad (\text{A.47})$$

Replacing the derivatives in the heat equation with (A.46) and (A.47) and considering only the heating, radiative cooling, and the conductive cooling for simplicity, the equation becomes

$$T_i^{m+1} = T_i^m + \left[H_i^m - A_i^m ((T_i^m)^4 - (T_0)^4) + \alpha_i^m \frac{T_{i-1}^m - 2T_i^m - T_{i+1}^m}{\Delta x^2} \right] \Delta t \quad (\text{A.48})$$

where H_i^m is the beam heating in, A_i^m the radiative cooling factors, and α_i^m is the diffusivity of heat in node m in time and i in space. This has to satisfy the stability condition at:

$$\alpha \frac{\Delta t}{\Delta x^2} < \frac{1}{2} \quad (\text{A.49})$$

B.2.2 Initial and Boundary Conditions

The temperature needs to be defined at the first time step at t^0 due to the time dependent part. The initial conditions could be defined as input in PyTT, or it will be $T_i^0 = 300$ K, which will be defined by default.

The temperature at the boundaries will be specified at each time step due to the spatial dependent part and the Dirichlet boundary conditions are considered for the specification as follows

$$\begin{cases} T(0, t) = 300 \text{ K} \\ T(L, t) = 300 \text{ K} \end{cases} \quad (\text{A.50})$$

B.3 COMSOL Multiphysics

COMSOL Multiphysics is a commercial software used for simulating and modeling various physical phenomena, since most of the physical phenomena are formulated as differential equations which needed to be solved analytically. A model has been made using COMSOL Multiphysics to estimate the thermal evolution of the wire scanner. COMSOL uses Finite Element Method for spatial discretization. FEM takes the domain on which the differential equation is solved and partitions it into many smaller regions called elements, whereby the points defining the intersection between such elements are called nodes. The differential equation is approximated on each of these nodes using a polynomial test function. FEM has the ability to handle domains that are of arbitrary shape, and the accuracy of the solution can be improved by increasing the number of elements or using higher-order polynomial functions. These polynomial functions, called basis functions, must have the important property of being equal to one at their respective node and zero otherwise [36].

Based on [24], the procedure starts by multiplying both sides of the heat equation by a test function ψ_j and integrating over the geometry domain, as given by

$$\frac{\partial T}{\partial t} \int_{\Omega} \psi_j dS = \int_{\Omega} H \psi_j dS - \int_{\Omega} A((T)^4 - (T_0)^4) \psi_j dS - \int_{\Omega} \alpha \nabla T \nabla \psi_j dS \quad (\text{A.51})$$

The approximate temperature can be expressed as

$$T_h = \sum_i T_i \psi_i \quad (\text{A.52})$$

where ψ_i is the basis function of the i^{th} node and T_i is the coefficient of the basis function that approximates the temperature T to T_h . Substituting (A.52) into (A.51) yields

$$\begin{aligned} \sum_i \frac{\partial T_i}{\partial t} \int_{\Omega} \psi_i \psi_j dS &= \int_{\Omega} H (\sum_i T_i \psi_i) \psi_j dS - \int_{\Omega} A((\sum_i T_i \psi_i)^4 - (T_0)^4) \psi_j dS \\ &\quad - \sum_i T_i \int_{\Omega} \alpha \nabla \psi_i \nabla \psi_j dS. \end{aligned} \quad (\text{A.53})$$

In this equation the coefficients T_i are unknown. If j goes from 1 to n , then we have a system of n equations and n unknown coefficients T_i . The system of equations could be obtained in the following for

$$\mathbf{A}\mathbf{T}_h = \mathbf{b} \quad (\text{A.54})$$

with \mathbf{A} is called the system matrix or the stiffness matrix which is a $n \times n$ matrix contains all the coefficients T_i in each equation j , \mathbf{T}_h is a vector of unknowns $=T_1, T_2, \dots, T_n$ and \mathbf{b} is a vector of dimensions 1 to n . According to the integral of (A.52) only overlapping functions of neighbor nodes would have non-zero values, which in turn would have non-zero values in the stiffness matrix.

The temporal discretization is built up using the backward difference formula method (BDF) which is formulated as follows

$$\sum_k^s a_k T^{m+k} = \Delta t B \left. \frac{\partial T}{\partial t} \right|_{t^{m+s}} \quad (\text{A.55})$$

where the coefficients a_k and B are constant are chosen according to the maximum possible order k and it could be found in [37, 38]

The time-marching scheme in COMSOL has an automatic control of the BDF order and the step length depending on the problem and the evolution of the solution with time and it varies between the second and fifth order of BDF .

C Result for SPS Beam limitations

Here are the thermal evolution of the other wires wire discussed in 5.2.

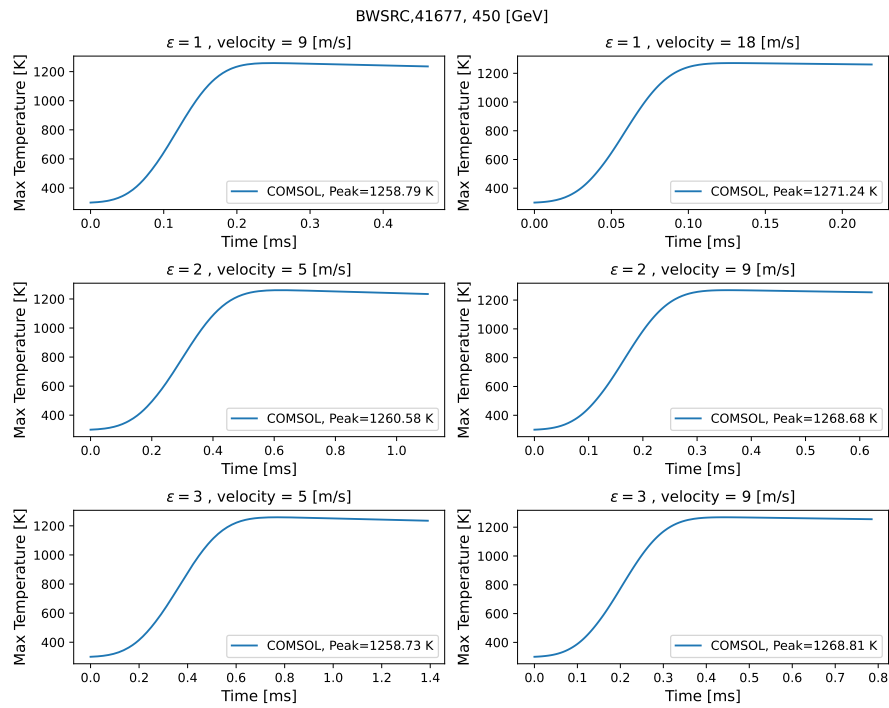


Figure 23: Thermal evolution of BWS,41677 with different velocities, normalized emittance, and beam size

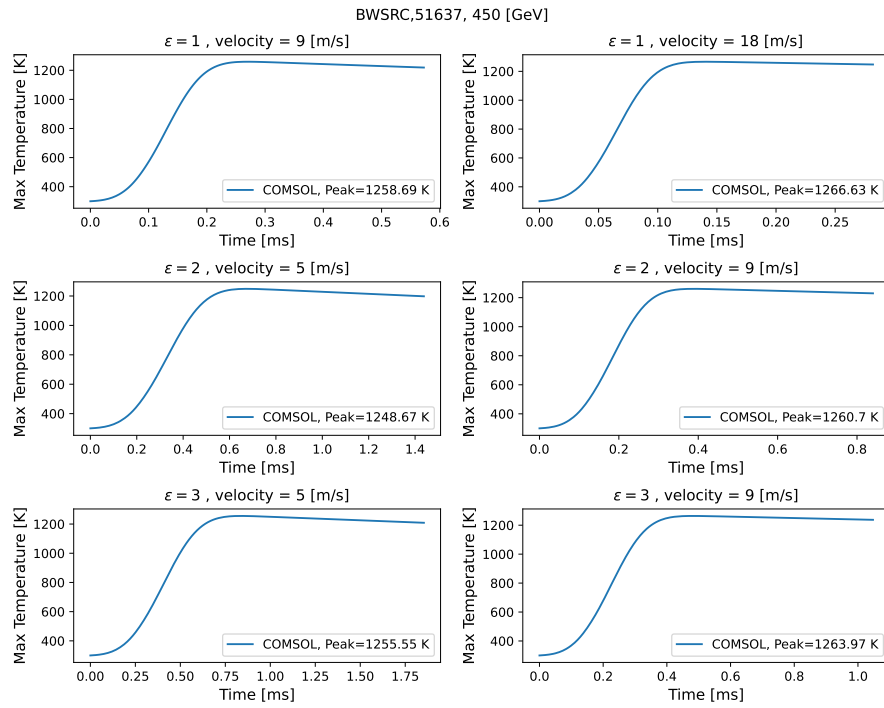


Figure 24: Thermal evolution of BWS,51638 with different velocities, normalized emittance, and beam size

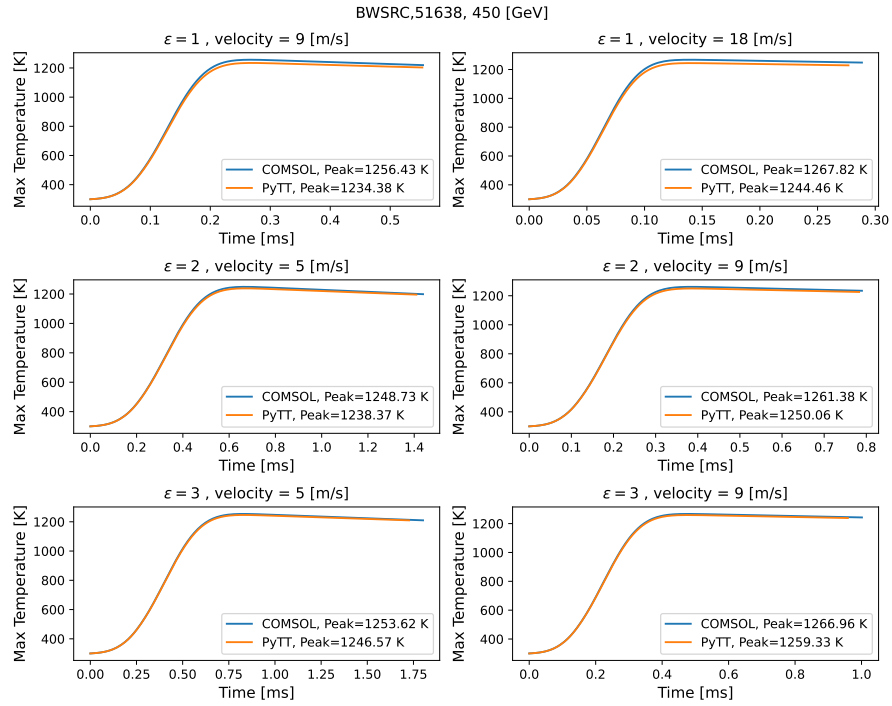


Figure 25: Thermal evolution of BWS,51638 with different velocities, normalized emittance, and beam size